2015

Chipless Radio Frequency Identification (RFID) Tag Utilizing Beamforming Technique

Ali Attaran
University of Windsor

Chipless Radio Frequency Identification (RFID) Tag Utilizing Beamforming Technique

By

Ali Attaran

A Dissertation
Submitted to the Faculty of Graduate Studies
through the Department of Electrical and Computer Engineering
in Partial Fulfillment of the Requirements for
the Degree of Doctor of Philosophy
at the University of Windsor

Windsor, Ontario, Canada

2015

Chipless Radio Frequency Identification (RFID) Tag Utilizing Beamforming Technique

by

Ali Attaran

APPROVED BY:

_____

Dr. K. El-Sankary, External Examiner
Dalhousie University

_____

Dr. A. Azab
Department of Industrial & Manufacturing Systems Engineering

_____

Dr. E. Abdel-Raheem
Department of Electrical and Computer Engineering

_____

Dr. K. Tepe
Department of Electrical and Computer Engineering

_____

Dr. R. Rashidzadeh, Co-supervisor
Department of Electrical and Computer Engineering

_____

Dr. R. Muscedere, Co-supervisor
Department of Electrical and Computer Engineering

March 25, 2015

Declaration of Co-Authorship and Previous Publications

DECLARATION OF CO-AUTHORSHIP

I hereby declare that this dissertation incorporates material that is the result of research conducted under the supervision of my supervisors, Dr. R. Rashidzadeh and Dr. R. Muscedere.

I am aware of the University of Windsor's Senate Policy on Authorship and I certify that I have properly acknowledged the contributions of other researchers to my dissertation, and I have obtained written permission from my co-authors to include the aforementioned materials in my dissertation.

I certify that this dissertation and the research results to which it refers are the product of my own work.

DECLARATION OF PREVIOUS PUBLICATION

I declare that this dissertation includes one published letter and four original papers that have been submitted for publication in peer reviewed journals as follows:

Dissertation Chapter	Publication Title/full Citation	Publication Status
Chapter 2	Attaran, R. Rashidzadeh, and R. Muscedere, "Chipless RFID tag using RF MEMS switch" *Electronics Letters* , vol.50, no.23, pp.1720,1722, 11 6 2014	Published
Chapter 3	A. Attaran, R. Rashidzadeh, and R. Muscedere, "Rotman Lens Combined with Wide Bandwidth Antenna Array for 60GHz RFID Application," *International Journal of Microwave and Wireless Technologies*, Cambridge University Press, 13pp, Dec 2014.	Passed the first round of review
Chapter 4	A. Attaran, R. Rashidzadeh, and R. Muscedere, "Rotman Lens Phase Error Reduction Using Constant Path Delay," submitted to *International Journal of RF and Microwave Computer-Aided Engineering*, *Wiley,* 17 pp, Feb 2015.	Submitted
Chapter 5	A. Attaran, R. Rashidzadeh, and R. Muscedere, "Novel 60-GHz Radio Frequency Identification Reader Using Passive Mixer," submitted to *Microelectronics Journal, Elsevier*, 18 pp, May 2014.	Submitted
Chapter 6	Attaran, R. Rashidzadeh, and R. Muscedere, "Programmable Chipless Radio Frequency Identification Tag Using RF MEMS Switches"	To be submitted

I certify that I have obtained a written permission from the copyright owners to include the above published materials in my dissertation. I certify that the above material describes

the work completed during my registration as graduate student at the University of Windsor.

I declare that, to the best of my knowledge, my dissertation does not infringe upon anyone's copyright nor violate any proprietary rights and that any ideas, techniques, quotations, or any other material from the work of other people included in my dissertation, published or otherwise, are fully acknowledged in accordance with the standard referencing practices. Furthermore, to the extent that I have included copyrighted material that surpasses the bounds of fair dealing within the meaning of the Canada Copyright Act, I certify that I have obtained a written permission from the copyright owners to include such materials in my dissertation.

I declare that this is a true copy of my dissertation, including any final revisions, as approved by my dissertation committee and the Graduate Studies office, and that this dissertation has not been submitted for a higher degree to any other University or Institution.

Abstract

This work is a paper based dissertation which presents a new method to design low cost chipless radio-frequency identification (RFID) tags using MEMS technology. The proposed chipless tag can be batch-fabricated using a basic MEMS fabrication process. The chipless tag can operate over a wide range of frequencies including the conventional UHF band for RFID applications. The elimination of the chip can reduces the tag price to the extent that it becomes an alternative solution to barcode labels. A prototype of the tag is implemented using a basic fabrication process and measurements are performed to validate its functionality. For the RFID reader, a direct conversion passive micro-mixer combined with a 180° ring hybrid coupler is realized to operate over the unlicensed 60 GHz frequency band. This is followed by a low phase error Rotman lens combined with a patch antenna array in each output port to support beam steering and increasing the communication range. Experimental measurements on a fabricated 3-bit chipless tag show that the tag can backscatter a unique identification code to an RFID interrogator.

Dedication

To my Dear Parents

Acknowledgement

There are many people that I owe my sincere appreciation for their generous help, guidance and contributions to completion of this doctoral dissertation.

First of all, I would like to express my gratitude to my advisors Dr. R. Rashidzadeh and Dr. R. Muscedere for their invaluable support, inspiration and commitment throughout the course of this work.

I am also grateful to the rest of my doctoral committee: Dr. K. Tepe and Dr. E. Abdel-Raheem from Electrical and Computer Engineering Department, Dr. A. Azab from Industrial & Manufacturing Systems Engineering Department, and Dr. K. El-Sankary from Dalhousie University for their time and attention in reviewing my dissertation, and their encouraging words and constructive criticism.

Finally, my deepest gratitude goes to my loving wife, mom, dad, sisters and brother. Without their generous love, support, and encouragement, this research work would have never come to a successful completion.

TABLE OF CONTENTS

Chapter 1

Introduction

In the first part of this work a novel chipless radio-frequency identification (RFID) tag which uses micro-electro-mechanical systems (MEMS) technology and a beamforming technique for 60GHz application is presented. The tag can also operate at the conventional UHF band for RFID applications and is implemented using a basic fabrication process. In the presented scheme, MEMS switches are used as programmable elements to support communication between the tag and RFID interrogators. The removal of traditional analog/digital components (ie. Chipless) allows for the overall reduction in costs such that it can be an alternative to printed barcode labels. The tag is implemented and tested using a simple MEMS fabrication process and E5061B 3k-3GHz ENA Series Network Analyzer. The S-parameters of the tag show better than 1dB loss and isolation of lower than -17dB

for a spectrum extending from 3 kHz to 3 GHz. In the implemented tag, a series of new low actuation voltage RF MEMS switches are designed and tested. Despite the progress in the design of RF MEMS switches, designing a low actuation voltage RF MEMS switch is still a challenging task. To overcome this problem, a small size RF MEMS switch utilizing a moving plate with multiple holes supported by a low spring constant beam is designed in this work.

Next, a direct conversion passive micro-mixer is realized for 60GHz RFID applications. In order to reduce the size, cost and complexity of the reader, the traditional method of using two separate paths is eliminated by a 180° ring hybrid coupler which sends and receives the signal using just one path. This ring coupler can provide a wide bandwidth while supporting a simple structure and can be easily fabricated. The designed coupler has a -3.1 dB insertion loss and better than -30 dB return loss at 60 GHz center frequency. The conversion gain of the passive microwave mixer (utilizing a flip-chip dual GaAs diode) is -7.47 dB.

This is followed by a new design technique and analysis for microstrip Rotman lens. In the proposed method, progressive phase delay is realized independent of the length of transmission lines to reduce the complexity of the design and improve the performance parameters. A Rotman lens has also been designed based on the presented technique which has 5 beam ports, 5 array ports, 4 dummy ports, and a footprint as small as 11 mm by 10.7 mm at a 60 GHz operational frequency. The simulation results indicate that the proposed

method as compared to the conventional design method reduces the phase error from 0.42 degree to 0.25 degree. The output array ports of the designed Rotman lens feed a wide bandwidth microstrip patch antenna array. This combination supports location positioning, covers a wide scanning angle and increases the communication range through a highly directive antenna array. The antenna array can provide high gain, directivity and bandwidth by taking advantage of the λ/4 microstrip transmission lines. While using the Rotman lens, the progressive phase delay can be realized independent of the transmission lines length to reduce the complexity of the design and improve the performance parameters. The λ/4 radial stubs are utilized to terminate the dummy ports which reduces the cost of fabrication since via holes are no longer required. It will also lower the cost of testing by eliminating the need for expensive connectors for the dummy ports.

Chapter 2

Chipless RFID tag using RF MEMS switch

Although RFID systems have successfully been implemented for many applications, RFID tags have not been able to replace barcode labels mainly due to the costs associated with the microelectronic chips in RFID tags. An array of antennas or multi-resonators is proposed as a chipless tag in the literature [1], however this solution requires operation at multi gigahertz frequencies to reduce the size of antenna elements. In this letter a new MEMS-based solution is presented which can operate at the standard UHF band for RFID applications.

II. PRINCIPAL OF OPERATION:

Communication between RFID UHF tags and interrogators is commonly performed through signal backscattering. In this method, the transmitted signal is backscattered to the

RFID reader when the tag antenna is connected to a small load or ground. When the tag antenna is open or connected to a large load, it does not radiate back the incoming signal. In fact the tag's control circuit simply turns on and off a switch between the tag's antenna and ground to communicate with readers. In a conventional UHF RFID tag, a chip is used to control the tag's switching activities and pattern the backscattered signal [2, 3].

In the proposed method in this letter, the backscattered signal is patterned by an array of MEMS-switching module. Each switching module can connect the tag antenna to the ground path for a short period of time to backscatter the incoming signal. Fig. 1 shows an implemented switching module which includes two MEMS switches with different pull-in voltages of V_1 and V_2. When the control voltage, V_{cntl} exceeds V_1 the first switch, SW_1, turns on and connects the antenna to ground. The antenna path to ground remains closed until the input voltage exceeds V_2 when the second switch, SW_2, turns on and connects node A to ground. As a result SW_1 is turned off and the antenna path to ground is opened.

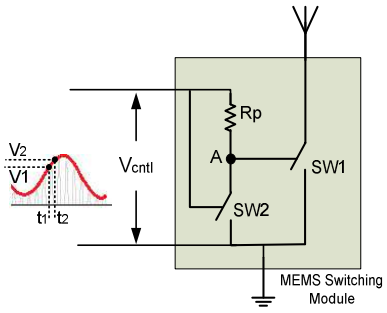

Fig. 1 One-bit MEMS switching module.

The antenna backscatters the interrogator's signal for a period of time when $V_1 < V_{cntl} < V_2$ and the antenna path to ground is closed. The MEMS module in Fig. 1 can be used to

communicate one bit information. A number of MEMS switching modules with different pull-in voltages can be utilized to communicate several bits of information. To communicate with tag, the amplitude of transmitted signals by readers has to be modulated. The voltage across the above switching module has to exceed the pull-in voltages of the implemented MEMS switches to ensure proper operation. However, the antenna of a conventional UHF RFID tag provides an open-circuit voltage of about 0.1-0.3V, which is not high enough to turn on a MEMS switch. To overcome this problem, reactive matching technique is utilized. Fig. 2 shows a simplified diagram of the proposed chipless RFID. It includes a receiving antenna which is represented by its equivalent circuit together with an envelope detector, two MEMS switches and a transmitting antenna. Such a basic structure can be used to communicate one-bit information by turning SW_1 on and off using the induced voltage across the receiving antenna.

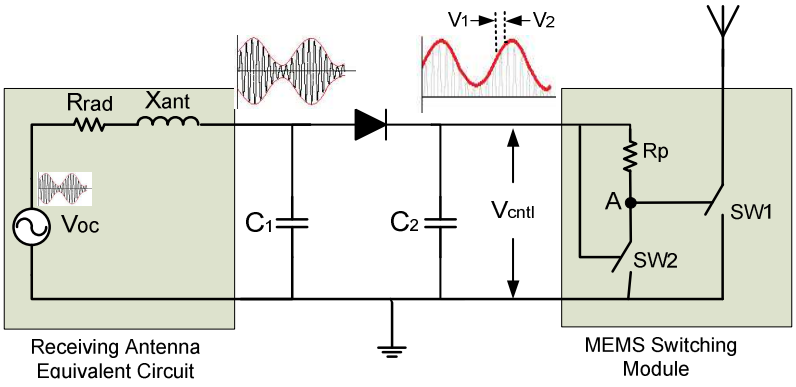

Fig. 2 Chipless tag using two MEMS switches to send one bit information through backscattering. The received signal is backscattered when $V_1 < V_{cntl} < V_2$.

The antenna reactance, X_{ant}, is matched with a capacitor, C_1 in Fig. 2, to increase the level

of voltage across the MEMS switches. It can be shown that at the resonant frequency, the voltage across C_1 is $\sqrt{Q}$ times higher than the induced voltage on the antenna, V_{oc}. Where Q is the quality factor of the RLC circuit formed by R_{rad}, X_{ant} and C_1. If the RLC components are selected properly, the voltage across C_1 can be high enough to turn on the MEMS switches.

III. N-BIT CHIPLESS PROGRAMMABLE TAG:

An N-bit chipless tag using 2N MEMS switches is presented in Fig. 3. The MEMS switches in each module are designed to turn-on at a particular time slot defined by their pull-in voltages. As a result, each switching module connects the antenna to the ground in a certain time slot. The MEMS switches can be designed to distribute N bits information over one period of the envelope signal transmitted by an RFID reader.

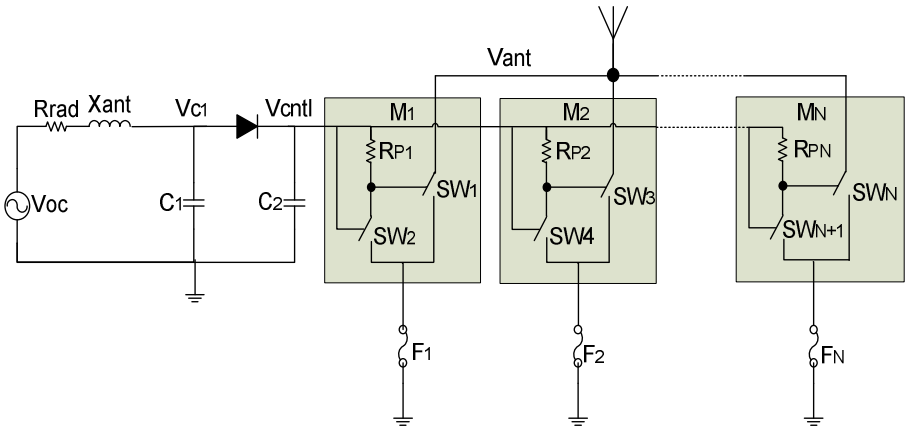

Fig. 3 Schematic diagram of an N-bit chipless tag.

The tag can be programmed to a unique backscattering pattern or code by burning fuses connected to the switching modules and break the paths to ground. A switching

module without the path to ground cannot backscatter the incoming signal and can be considered a logical low.

Tag Implementation: All the components in Fig. 3, except the diode, can be implemented using a basic fabrication process containing two metal layers and one resistive layer. To implement the tag, MEMS switches with different pull-in voltages are needed. There are different structures to implement a MEMS switch, among them cantilever switch supports a relatively low pull-in voltage. The pull-in voltage, $V_{pull-in}$, of a MEMS switch can be calculated from

$$V_{pull-in} = \sqrt{\frac{8K_z g_0^3}{27W\varepsilon_0}} \quad (1)$$

Where K_z is the spring constant, g_0 is the gap between metal plates, W is the area of the pads and ε_0 is the air permittivity. Table 1 shows the dimensions of the MEMS switches used to encode 3-bit information. The pull-in voltages of the implemented switches vary from 0.7V to 1.5V.

IV. SIMULATION AND MEASUREMENT RESULTS:

Fig. 4a indicates the layout of the implemented MEMS switch with pull-in voltage of 1.5V. The fabricated MEMS switch in Fig. 4b which is connected to the test was connected to a commercially available RFID UHF tag antenna. Simulation results using ADS software and measurement results using E5061B network analyzer from Agilent and SemiProbe Lab assistant are shown in Fig. 4c. It can be seen that there is a good agreement between the

simulation and measurement results. The deviation between the measured and simulated responses for frequency range of 1.5GHz to 2GHz is due to the loss of cables used for measurement. The results in Fig. 4a indicate that the tag antenna can backscatter the incident signal at about 910MHz when the switch is ON. A 3-bit chipless tag based on the diagram presented in Fig. 3 with an identification code of "101" was implemented to test the tag response. The fabricated MEMS switching module for the 3-bit chipless tag is shown in Fig. 4d. A 910MHz carrier signal modulated with a 1 KHz sinusoidal waveform with an amplitude of 0.2V was applied to the circuit. The tag's matching circuit was designed to increase the level of the input signal by a factor of about 12. The envelop detector demodulates the transmitted signal and provides the switching modules with a low frequency signal. The amplitude of the low frequency signal as shown in Fig. 5 exceeds the threshold voltages of all MEMS switches. This allows the switching modules to properly pattern the backscattered signal. The output signal in Fig. 5 shows that the tag detects the incoming signal and backscatters its unique "101" identification code. The total power consumption of the designed 3-bit chipless tag is about 24μw.

Assuming an isotropic UHF RFID integrator with 30dBm transmitted power and a tag antenna with an effective area of $A_e = \lambda/4\pi$ at 910MHz, the read range for the implemented tag is about 6.5m. Where λ is the wavelength of the signal transmitted by reader. The read range can be further increased if the MEMS switches are optimized for power consumption. In the proposed MEMS based RFID tag, the maximum number of tags

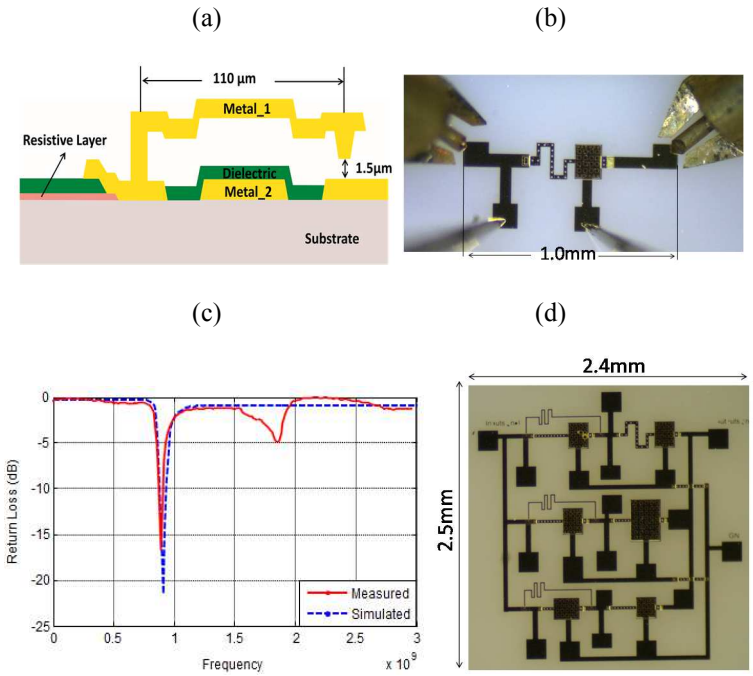

Fig. 4 (a) Layout of the MEMS switch with 1.5V pull-in voltage. (b) Fabricated MEMS switch for one-bit information under test. (c) Measurement and simulated return loss of the tag antenna when the switch is ON. (d) Fabricated MEMS switching module for 3-bit chipless tag.

Table1. Dimensions of the implemented switches

	Restoring Spring Length×Width (µm)	Actuation Pad Length×Width (µm)
SW_1	700×30	190×220
SW_2	140×30	285×400
SW_3	235×30	190×220
SW_4	235×30	190×200
SW_5	135×30	190×200
SW_6	110×30	240×200

that can be simultaneously identified depends on the number of MEMS switching modules in a tag. Each switching module represents one bit information and the number of tags that can be uniquely identified is calculated from 2^n-1. Where n is the number of switching

modules. For the fabricated prototype with three switching modules, seven tags can be concurrently identified. It has to be noted that the number of switching modules cannot be increased arbitrary. Increasing the number of switching modules raises the power consumption and the required forward link budget which limits the read range in return. As compared to the available UHF RFID tags, the fabrication process of the MEMS based RFID tag is much easier and less expensive. However, the proposed tag supports a limited number of bits for communication and the transmitted information is not encrypted. These shortcomings can be addressed by designing a network of power efficient switching modules using multi-pole MEMS switches.

II. CONCLUSION:

This letter presents a new method to implement low cost chipless RFID tags using MEMS technology. The proposed tags can be batch-fabricated using a basic MEMS fabrication process. The elimination of the chip, which accounts for the major portion of the RFID tag costs, can reduce the tag price to become an alternative to barcode labels. Simulation and measurement results using a 3-bit chipless tag indicate that the tag can backscatter a unique identification code to an RFID interrogator.

Acknowledgments: The authors would like to thank the research and financial supports received from Natural Sciences and Engineering Research Council (NSERC) of Canada and CMC Microsystems.

(a)

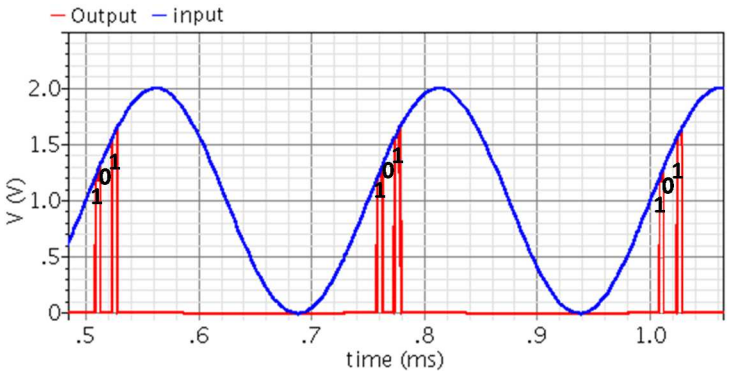

(b)

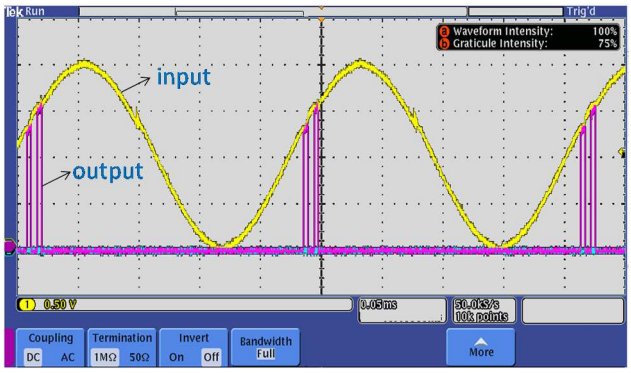

Fig. 5 Transient response of the chipless tag using 3-bit MEMS switching modules. (a) Simulation results for a tag with 101 identification code. (b) Measurement results.

REFERENCES

1. Vena, A., Perret, E., Tedjini, S., Tourtollet, G. E. P., Delattre, A., Garet, F., Boutant, Y.: 'Design of Chipless RFID Tags Printed on Paper by Flexography', IEEE Trans. on Ant. and Propag., 2013, 61, (12), pp. 5868–5877.

2. Dobkin, D. M.: 'The RF in RFID: Passive UHF in Practice' (Newnes is an imprint of Elsevier, 2008)

3. Mirzaee, M., Virdee, B.S.: ‘Realisation of highly compact planar lowpass filter for UWB RFID applications’, Electron. Lett., 2013, 49, (22), pp. 1396–1398.

Chapter 3

Rotman Lens Combined with Wide Bandwidth Antenna Array for 60GHz RFID Applications

The growth of millimeter-wave identification system (MMID) is found vital due to higher bandwidth requirement, interference free spectrum, compact size, low power consumption. A MMID reader can be used for high data rate applications such as the next generation of WPAN/LAN, intelligent highways and human implants. MIMD systems are also cost effective and support small size identification tags [1-4]. The 60 GHz band is an unlicensed spectrum with a 7 GHz bandwidth (57-64 GHz) which can support high-speed and high-capacity wireless links. It is considered to be an interference free band due to the high O_2 absorption of approximately 14 dB/km. Although such a high attenuation factor limits the communication range, it also reduces the effect of interferences significantly and increases the security. The 60GHz band supports a compact size reader and tag. A dipole antenna on a Low Temperature Co-fire Ceramic (LTCC) substrate at this frequency is almost 25 times

smaller than its counterpart at 2.4 GHz, shown in Fig. 1. In fact the entire reader can be implemented on a single compact sized wafer.

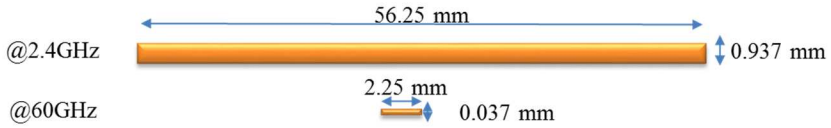

Fig. 1. Dipole antenna at 2.4GHz and 60GHz using the same substrate material.

Among the various beamforming methods, a technique utilizing a Rotman lens is a viable solutions due to its ease of implementation and integration with available fabrication technologies for integrated circuits. A properly designed Rotman lens can readily support the required beam scanning range and resolution to meet the design objectives. A 60 GHz Rotman lens feeding a microstrip patch antenna array can increase the communication range while supporting location positioning.

In this paper, a low phase error Rotman lens combined with a microstrip patch antenna array is proposed as a transceiver for high-speed applications. In the proposed scheme, $\lambda/4$ radial stubs are utilized as virtual ground to terminate dummy ports. The lens and antenna array can be fabricated back to back using a multilayer LTCC substrate to reduce the size of the reader. Simulations were carried out using High Frequency Structure Simulator (HFSS) and Agilent CAD tools (ADS, Genesys and Empro) for 3D full-wave simulations to ensure the accuracy of the results and to optimize the geometry of the lens and antenna array.

II. SERIES FED WIDE BANDWIDTH MICROSTRIP PATCH ANTENNA ARRAY

Series fed microstrip patch antenna arrays are known for their high gain and directivity, low profile and ease of implementation with low weight [5]. Microstrip patches are connected in series along their resonant dimension via an arrangement of $\lambda_g/2$ high impedance microstrip transmission lines. Therefore, all patches are in the same phase and can resonate at the desired designed frequency. The associated losses of this antenna types is lower than other configurations due to the compactness of the feed arrangement and therefore most suitable choice for linear arrays. The main drawbacks of series fed antenna arrays are (a) large impedance variation, (b) main beam direction over a band of frequencies [6-7] and (c) narrow radiation bandwidth. In this work the radiation bandwidth is improved four times using periodic open ended $\lambda_g/4$ stubs in compare to the same array without using radial stubs.

Direction of the main beam and the scan sensitivity can be determined from (1-2) equations [6]:

$$d\sin\theta + \sqrt{\varepsilon}l = \lambda = \frac{c}{f} \tag{1}$$

$$\frac{\partial\theta}{\partial f} = -\frac{c}{df^2\cos\theta} \tag{2}$$

where d is element spacing, l is the length of the transmission line joining the successive elements, c is the velocity of light, f is the frequency of the operation and θ is the beam-pointing angle measured from the anticipated direction. In order to reduce the sidelobe level, the width of each patch element, (in the nonresonant direction), can be adjusted to

control the radiation resistance and the required amplitude distribution. Each resonant element in this configuration can be realized as a two port microstrip rectangular element with ports located on its nonresonant edges.

Radiated power of a resonant element can be determined from its excitation. The reflection at each junction should be taken into consideration in the calculation of the available power for each radiator. The power radiated by the *n*th resonant element in the series fed array configuration can be calculated from (3) [6]:

$$V_{rn}^2 = P_{rn} = g_n(1-g_{n-1})(1-g_{n-2})\ldots (1-g_1)(1-|\Gamma_1|^2)(1-|\Gamma_2|^2)\ldots(1-|\Gamma_n|^2) \quad (3)$$

where the normalized radiation conductance, g_r, and reflection coefficient, Γ, for a given element are obtained from $g_r = Z_0/R_{rad}$ and $\Gamma_n = (Z_{\text{in}n} - Z_{fl})/(Z_{\text{in}n} + Z_{fl})$. R_{rad} is the radiation resistance of the patch element, Z_0 is the characteristic impedance of the feed line, $Z_{\text{in}n}$ is the input impedance at the *n*th junction and Z_{fl} is the feed line impedance. From the insertion phase of the patch and connecting transmission line, the phase distribution across the array can be obtained. The relative phase and electrical length at each element of the array can be calculated from the wavelength in the patch and feed line. The radiation pattern and array factor can be calculated as phase and amplitude are known.

Instead of using conventional step methods or tapers, three open ended $\lambda_g/4$ stubs in each $\lambda_g/8$ portion of the transmission lines are used in order to match the patches with exciting ports and increase the impedance bandwidth of the series fed microstrip patch

antenna array. These capacitive stubs linearize and lower the characteristic impedance of the array to a constant value. They are not required to be 180^o electrical length since they do not resonant. More pattern control in the E-plane is possible by controlling the phase of edges using stubs with different lengths. The bandwidth of a series fed microstrip patch antenna increases significantly if periodic open ended $\lambda_g/4$ stubs are used to ensure a constant Bloch wave characteristic impedance [7].

To design a wide bandwidth patch antenna array the characteristic impedance of the patches should be equal to the characteristic impedance of the feed lines [8-10]. Each section of the loaded transmission line can be modeled as a high impedance transmission line series with a low impedance transmission line. Fig. 2, shows a schematic diagram of an eight elements series fed microstrip patch antennas including $\lambda_g/2$ transmission lines to connect these elements and $\lambda_g/4$ open ended transmission lines. This array is designed and simulated on the top layer of a multilayer LTCC substrate with dielectric constant (ε_r) of 7.8 and thickness of 121μm. Fig. 3 presents the gain and directivity of series fed microstrip patch antenna array with maximum of 18dB and 25dB, respectively. S_{11} and Voltage Standing Wave Ratio (VSWR) of the series fed microstrip patch antenna array are shown in Fig. 4.

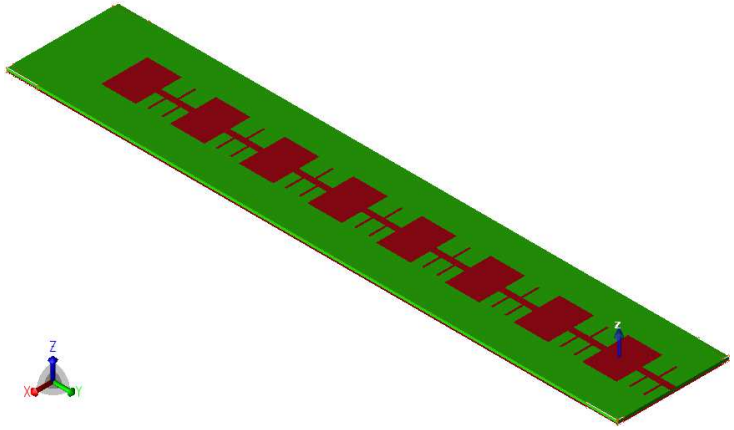

Fig. 2. Series fed microstrip patch antenna array

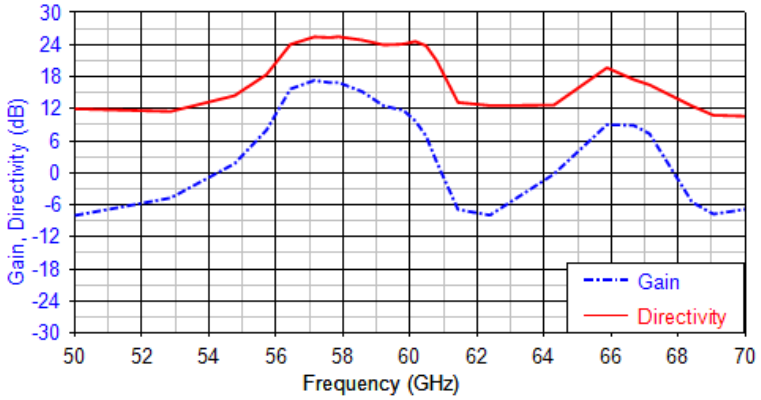

Fig. 3. Gain and directivity of series fed microstrip patch antenna array

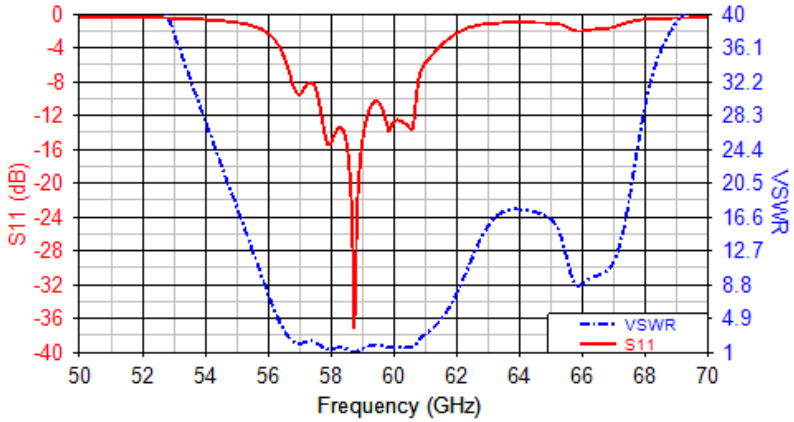

Fig. 4. S_{11} and VSWR of the of Series fed microstrip patch antenna array

3D and 2D radiation patterns of a single microstrip patch antenna array at the center frequency of 58.57 GHz are presented in Fig. 5. The radiation patterns remain generally constant and symmetric across the matched impedance bandwidth.

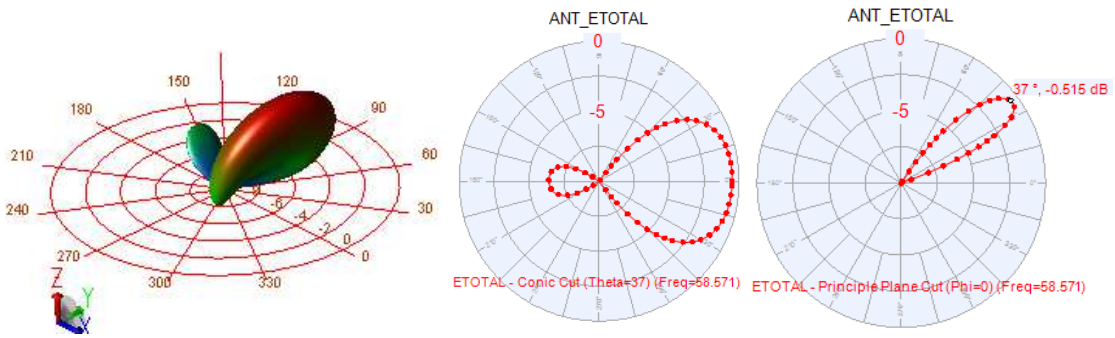

(a) (b) (c)

Fig. 5. (a) Full 3D radiation pattern of a single microstrip patch antenna array at 58.57 GHz center frequency, (b) Conic cut, sweep phi, theta 37°, (c) E-Plane, sweep theta, phi=0°

III. MICROSTRIP ROTMAN LENS WITH SMALL PHASE ERROR

Passive beamforming is a powerful method for location positioning at the millimeter frequency range. Increasing the directivity with a microstrip patch antenna array at the millimeter wave frequency band lowers the design complexity and reduces the costs. A Rotman lens is designed at the center frequency of 60 GHz for RFID applications in this work. Five beam ports were chosen to allow for a wide range of beam steering with a small amount of phase error. A scan angle of 30° has been selected to cover an azimuthal angle of 60° at a -6 dB antenna radiation pattern to support a wide scanning capability. The antenna beam pattern is chosen to be approximately 15° at -3 dB to allow a beam overlap. The array element spacing along the outer contour was chosen to be $0.5\lambda_0$. Element

spacing determines the microstrip patch antenna row spacing and eventually the desired beamwidth.

To keep the geometry compact, the scan angle φ has been selected to be the same as the focal angle α. To implementation the structure, the same substrate with a dielectric constant (ε_r) of 7.8 and thickness of 121μm as the series fed microstrip patch array antenna is used. The LTCC substrate has a loss tangent of 0.001. The low line losses as well as competitive manufacturing costs are the main advantages of LTCC for RF and microwave applications.

After the initial design objectives were set, the lens geometry was simulated with a Finite Difference Time Domain (FDTD) simulator and the results were confirmed with a Finite Element Method (FEM) analysis. The design parameters including geometric dimensions and losses were then optimized using sidelobe levels, phase errors, and sidewall curvature as cost functions. A 3D view of the designed lens is shown in Fig. 6.

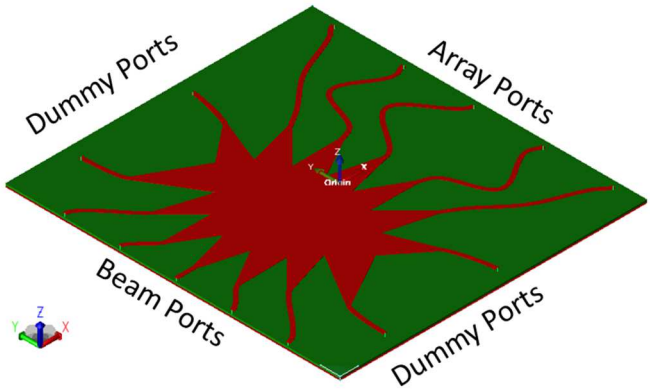

Fig. 6. 3D view of the designed Rotman lens geometry

The main parameter for the Rotman lens is its array factor which presents the beam direction, angle and level of side lobes. The array factor is shown in Fig. 7a for different

beam port excitation which has side lobes of less than -12 dB at a 60 GHz center frequency. The array factor analyses indicate that medium beam transmission lines and routed medium array transmission lines with small tapered flare angle are the best choices to lower the side lobes level.

An important design factor is the accuracy in the beam steering and the maximum phase error associated with the different beam ports excitation. Phase error can be determined by comparing electrical lengths along two different paths from a given beam port through the lens [11-14]. The first path travels along each of the off axis array ports. As for the second path, it begins at the same beam port but travels through the array curve center.

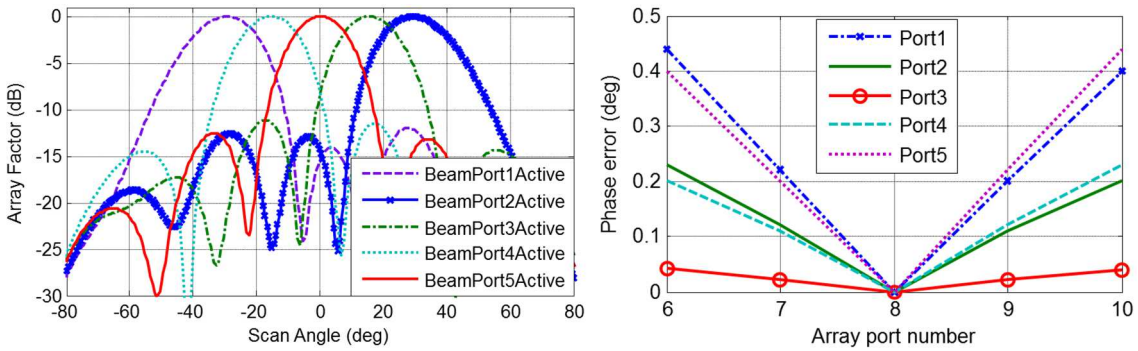

(a) (b)

Fig. 7. (a) Synthesized Array factor for beam ports, (b) Beam to array phase error for different beam ports excited.

The beam to array phase error for all ports of the proposed scheme is shown in Fig. 7b; it is always zero for the center array port as it is the calculation reference point. All beam and array port locations are optimized to produce minimum phase errors. The maximum beam to array phase error for all beam ports was found below 0.45˚, and the average phase error is lower than 0.25˚ which is a considerable improvement compared to the reported

phase error in other works [15-16].

A. Terminating the dummy ports using λ/4 radial stubs

To further reduce the costs of fabrication, $\lambda/4$ radial stubs, instead of via hole through the substrate, are used to terminate the dummy ports of the proposed lens. This also reduces the costs of testing by eliminating the need for costly connectors for each dummy port during the test phase. Fig. 8a shows the top view of the proposed lens and Fig. 8b shows the array factor of the proposed Rotman lens with radial stubs for dummy ports termination. In comparison to the via hole termination shown in Fig. 6 the center beam ports is excited here.

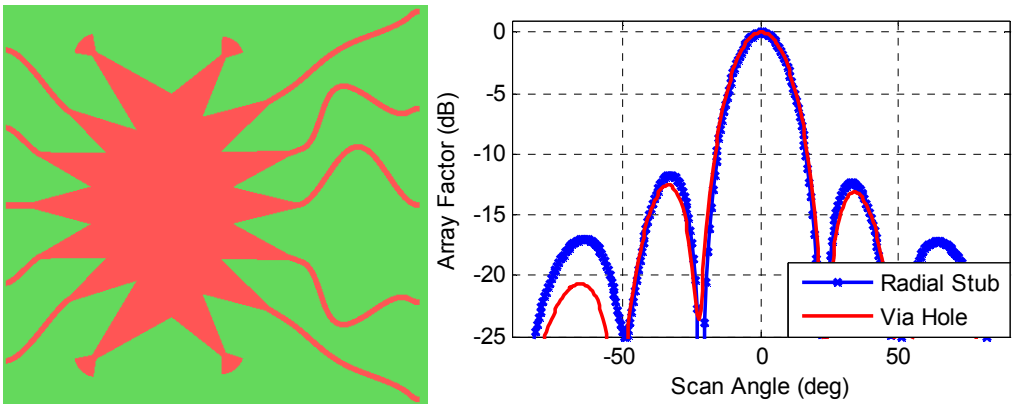

(a) (b)

Fig. 8. (a) top view of the proposed lens using radial stub for terminating the dummy ports, (b) array factor using radial stub and via hole through substrate.

The array factors of the lens for the center beam port show that the main lobes are unaffected while main side lobe levels increased almost by 0.5 dB. In addition to the cost reduction, the $\lambda/4$ radial stub reduces the area overhead. The stubs are connected in series with 50 Ω tapers. The geometry calculation of the radial stub is illustrated below in Fig. 9.

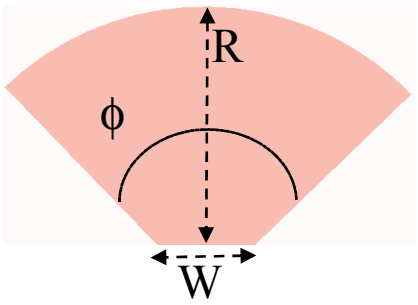

Fig. 9. Geometry of the radial stub

The width, W, of the stub is set to be 50 Ω to match with the taper of the lens shown in Fig. 9. The length, R, is chosen to be equal to $\lambda/4$, with this length an open circuit stub acts as a short circuit. The angle, ϕ, is limited to a range: $\phi_{min} < \phi < 170°$. These limitations support practical geometries. The minimum angle, ϕ_{min}, is limited to where the chord across the arc is less than W and can be calculated from: $\phi_{min} = 2 \times \arcsin(0.5W/R)$. The ϕ is chosen to be 70° to meet the design requirement while reducing side lobe levels.

IV. MICROSTRIP SERIES ANTENNA ARRAY FED BY THE ROTMAN LENS

One approach to reduce the costs of an RFID reader or wireless communication systems is to employ Micro Electro Mechanical Systems (MEMS) technology utilizing low cost materials. A Microwave beamformer, such as a Rotman lens, offers a path delay mechanism to form the desired beamforming without any extra analog or digital circuitry. The lens can be combined with a highly directional series-fed antenna array utilizing the same technology and substrate to ease the packaging complexity and reduce the fabrication costs. These two components provide an inexpensive and compact solution to implement

a 60 GHz transceiver. Fig. 10 shows the geometry of the proposed lens connected to a series fed microstrip patch antenna arrays. Fig. 11 and 12 present the gain, directivity, return loss and voltage standing wave ratio of the proposed lens connected to the arrays of antenna. In a uniformly excited planer antenna array with equal space of $\lambda/2$, the directivity and gain are highly depended on the element spacing and the number of elements.

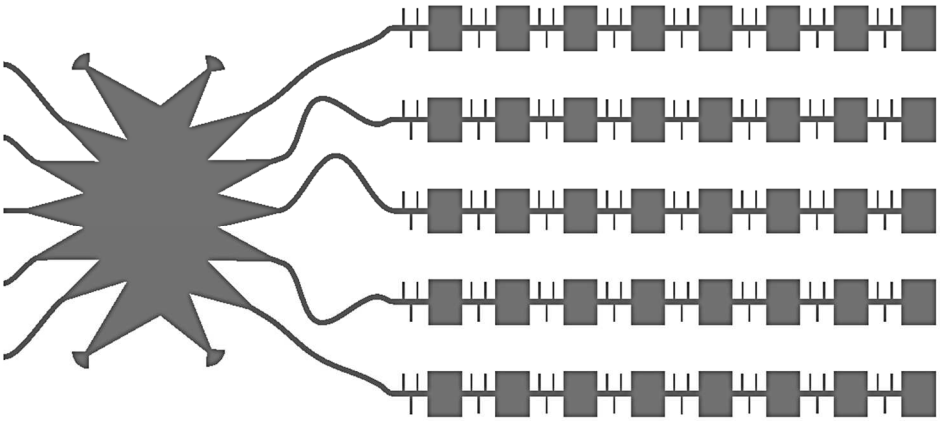

Fig. 10. Rotman lens connected to 5 series fed microstrip 8 patch antenna arrays

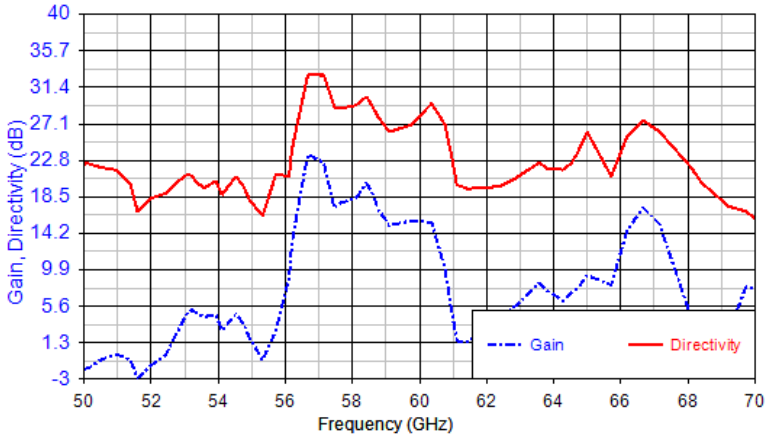

Fig. 11. Gain and directivity of the planner antenna connected to Rotman lens

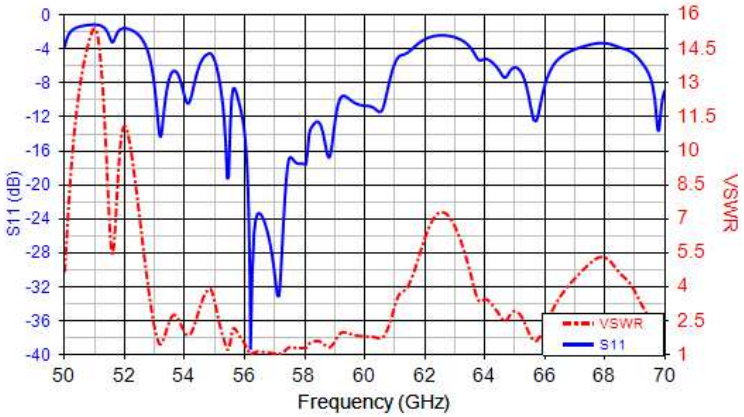

Fig. 12. S_{11} and VSWR of the planner antenna connected to Rotman lens

Far-field 3D and 2D radiation patterns of a Rotman lens combined with five microstrip patch antenna arrays at a center frequency of 58.57 GHz for an excited center beam port are presented in Fig. 13.

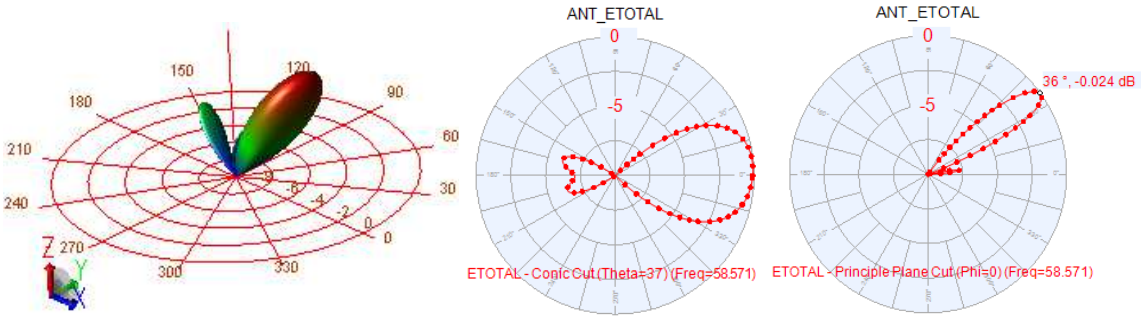

(a) (b) (c)

F

Fig. 13. (a) Full 3D radiation pattern of a Rotman lens combined with five microstrip patch antenna arrays at 58.57 GHz center frequency, (b) Conic cut sweep phi, theta 37°, (c) E-Plane, sweep theta, phi=0°

A. A Fabrication Alternative

Wafer area costs could further be reduced by fabricating the Rotman lens and antenna back to back on different sides of multilayer LTCC substrate. This approach enhances the compactness of the whole package considerably as most of the area is consumed by the

antenna especially if the number of patches are increased in the arrays; however the fabrication cost increases due to existing of many via holes through the substrate. From Fig. 10, for an array of eight microstrip patch antennas, the back to back design approach would cut the wafer size in half. The transition between layers can be done either electrically using a via or magnetically coupled slots. The power loss between layers is critical because it can reduce the efficiency of the entire system. To minimize this effect, via holes in a coaxial structure are realized to follow the fabrication process rules of the multilayer LTCC substrate. Fig. 14 shows the insertion loss and the return loss of a via hole using two 121μm layers of LTCC substrate at the center frequency of 60GHz.

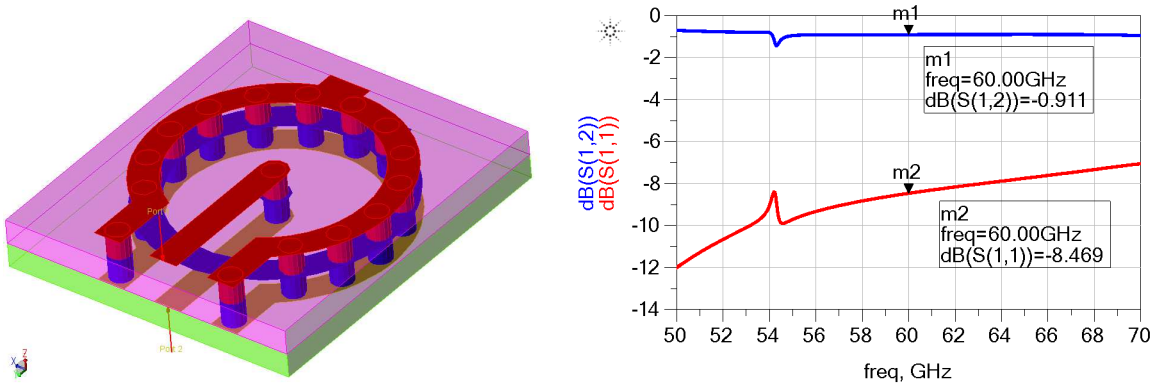

(a) (b)

Fig. 14. (a)Two layer coaxial via hole structure, (b) insertion and return losses of the coaxial via hole

V. CONCLUSION

A new design technique to realize an efficient microstrip Rotman lens combined with a wide bandwidth patch antenna array for 60 GHz applications is presented in this work to support location positioning and increase the communication range through beam steering. The progressive phase delay is realized independent of the length of transmission lines to

reduce the design complexity while improving the phase error. A wideband microstrip patch antenna array is developed with high gain, directivity and bandwidth using $\lambda/4$ microstrip transmission lines. Four radial stubs are used as virtual grounds to terminate the dummy ports instead of via holes in the Rotman lens to reduce the costs of fabrication and test.

ACKNOWLEDGMENTS: The authors would like to thank the research and financial supports received from Natural Sciences and Engineering Research Council (NSERC) of Canada and CMC Microsystems.

REFERENCE

1. Pursula, P.; Karttaavi, T.; Kantanen, M.; Lamminen, A.; Holmberg, J.; Lahdes, M.; Marttila, I.; Lahti, M.; Luukanen, A.; and Vähä-Heikkilä, T.: 60-GHz Millimeter-Wave Identification Reader on 90-nm CMOS and LTCC, Microwave Theory and Techniques, IEEE Transactions on, April 2011 vol.59, no.4, pp.1166-1173.

2. Pursula, P.; T. Vaha-Heikkila, Muller, A.; Neculoiu, D.; Konstantinidis, G.; Oja, A.; and Tuovinen, J.: Millimeter-Wave Identification—A New Short-Range Radio System for Low-Power High Data-Rate Applications, Microwave Theory and Techniques, IEEE Transactions on, Oct. 2008 vol.56, no.10, pp.2221-2228.

3. Pursula, P.; Donzelli, F.; and Seppa, H.: Passive RFID at Millimeter Waves, Microwave Theory and Techniques, IEEE Transactions on, Aug. 2011, vol.59, no.8, pp.2151-2157.

4. Ijaz, B.; Roy, S.; Masud, M.M.; Iftikhar, A.; Nariyal, S.; Ullah, I.; Asirvatham, K.; Booth, B.; Braaten, B.D.: A series-fed microstrip patch array with interconnecting CRLH transmission lines for WLAN applications, Antennas and Propagation (EuCAP), 2013 7th European Conference on, April 2013 , pp.2088-2091, 8-12.

5. Wu, W.; Yin, J.; and Yuan, N.: Design of an Efficient X-Band Waveguide-Fed Microstrip Patch Array, Antennas and Propagation, IEEE Transactions on, July 2007, vol.55, no.7, pp.1933-1939.

6. Garg, R., Bhartia, P., Bahl, I. J., & Ittipiboon, P. (2001). Microstrip Antenna Design Handbook. Artech House, Boston, London.

7. Strickland, P.C.: Series-fed microstrip patch arrays with periodic loading, Antennas and Propagation, IEEE Transactions on, Dec 1995 vol.43, no.12, pp. 1472-1474.

8. Gong, J.; and Volakis, J. L.: An efficient and accurate model of the coax cable feeding structure for FEM simulations, Antennas and Propagation, IEEE Transactions on, Dec 1995 vol.43, no.12, pp.1474-1478.

9. Casares-Miranda, F. P.; Viereck, C.; Camacho-Penalosa, C.; and Caloz, C.: Vertical microstrip transition for multilayer microwave circuits with decoupled passive and active layers, Microwave and Wireless Components Letters IEEE, July 2006 vol.16, no.7, pp.401-403.

10. Lafond, O.; Himdi, M.; Daniel, J. P.; and Haese-Rolland, N.: Microstrip/ thick-slot/microstrip transitions in millimeter waves, Microw. Optical Tech. Lett., July 2002 vol. 34, no. 2, pp. 100–103.

11. Rotman, W.; and Turner, R. F.: Wide-angle microwave lens for line source applications, Antennas and Propagation, IEEE Transactions on, 1963, 11, (6), pp. 623-632.

12. Hall, LT.: Broadband monolithic constrained lens design, Ph.D. thesis, The University of Adelaide, 2009.

13. Dong, J.: Microwave lens design: optimization, fast simulation algorithms, and 360-degree Scanning techniques, Ph.D. thesis, the Virginia Polytechnic Institute and State University, 2009.

14. Singhal, P. K.; Gupta, R. D.; and Sharma, P. C.: Recent Trends in Design and Analysis of Rotman-Type Lens for Multiple Beamforming, Int. J. RF and Microwave Computer Aided Engineering, CAE8, 1998, pp. 321-338.

15. Lee, W.; Kim, J.; and Yoon, Y. J.: Compact two-layer Rotman lens-fed microstrip antenna array at 24 GHz', IEEE Trans. Antennas Propag., 2011, 59, (2), pp. 460-465.

16. Lee W, Kim J, Cho CS, and Yoon Y J, 'A 60 GHz Rotman lens on a silicon wafer for system-on-a-chip and system-in-package application', in IMS. IEEE Conf., September 2009, pp. 1189-1192.

Chapter 4

Rotman Lens Phase Error Reduction Using Constant Path Delay

Passive beamformers are commonly used to lower design complexity and reduce the cost of microwave systems. Conventional passive beamformers such as Rotman lens, as compared to microelectronic based beam formers, offer a number of advantages due to their true time delay (TTD) characteristics, multibeam capabilities, and ease of integration with planar antenna and beam control circuitry. Using Rotman lens as a beamformer reduces system complexity while offering superior performance and smaller system size [1-3].

Conventional Rotman lens fabrication includes etching of a conducting material on a printed circuit board or a Duroid substrate. Individual ports are then excited using coax, microstrip, waveguide or aperture coupled feeds. The reproducibility of the devices implemented using this method is rather poor while the integration and packaging issues are easy to handle. In recent years, low temperature co-fired ceramic (LTCC) based

microwave devices have gained momentum. LTCC has a very low loss tangent and exhibits excellent characteristics as a starting substrate for microwave devices. LTCC technology supports implementation of different microwave components such as Rotman lens, antenna array, coupler, Rat-Race mixer and MEMS based RF switches. Additionally, multilayer LTCC substrate offers easy integration with other microelectronic circuits such as low pass filters, active or passive mixers and also wideband power amplifiers [4, 5]. As a result, it is possible to realize a complete transceiver using LTCC technology in a compact integrated system.

This paper presents a new design methodology for Rotman lens beamformer which reduces the design complexity and improves performance parameters. The proposed lens is designed and simulated using High Frequency Structure Simulator (HFSS), XFDTD and EMPRO CAD tools to conduct 3-D full wave electromagnetic analysis. Simulation results indicate improved performance parameters including array factor, phase error, cross talk or isolation, spill-over power coupling and beam pattern.

Various implementation methods such as microstrip, waveguide, synthesized dielectric slab with varying permittivity regions have been presented in the literature [2, 6]. Rotman lens is widely implemented using microstrip technology due to many benefits such as flexible structure, simple fabrication process, high power support ability, wide bandwidth and low cost [7-9]. In [7], compact two layer Rotman Lens with microstrip antenna array has been proposed. To reduce conductor loss, dielectric slab Rotman Lens is developed in

[3]. In [1], a thin layer of Sio2 is used to suppress the surface wave penetration into a high resistivity silicon.

In this paper, a new design technique which uses a constant path delay to minimize phase error is presented. The rest of the paper is organized as follows. Section II covers the operation principle of Rotman lens, followed by details of the proposed design technique in section III. Section IV covers the design details. Simulation results for the implemented Rotman lens is presented in section V. A microwave beamformer composed of the Rotman lens and an array antenna is covered in section VI and finally conclusions are discussed in section VII.

II. Operation Principle of Rotman Lens

A Rotman lens is a passive beamforming device with a number of input ports called beamports. It is used to feed a radiating element and control its beam direction by selective excitation of input ports. A typical Rotman lens, supports three major operation regions of (a) a semi-circular focal arc that traces the contour of the beam ports, (b) a curved line called the inner contour that traces the contour of the array ports, and (c) a straight line known as the outer contour that depicts the position of the radiating elements. The semi-circular focal arc is sometimes modified slightly to be elliptical to reduce aberration, phase error and sidelobes of the array factor [9]. Additional dummy ports are added on the side walls to minimize reflection. The beamforming principle of Rotman lens can be qualitatively described with the aid of Fig. 1. For the lens shown in Fig. 1a. any signal

incidents at the feed element a travels the same distance to reach the radiating elements at e and g. Thus the signals arrive in-phase at these points. These in-phase signals are then fed to the microstrip patch antennas to radiate a beam in the broadside direction. If the location of the feed element a is shifted to a new position to make an angle of α with the receiver at the center location c, any signal originating from location a will travel a shorter distance to reach the antenna at location e and a longer distance to reach the antenna at location g as shown in Fig 1b. Consequently, their arrival time at antennas located at e, f and g will be different. In other words, there will be a progressive time delay in signal arrival at locations e to f to g. In this case, the beam is steered in the direction of α as shown in Fig 1b. The antenna at location e radiates first as the signal arrives at this location ahead of the others. Antenna f radiates as the second radiator and antenna g becomes the third one to radiate. By appropriate positioning of the feed points and array ports in the contours, this progressive time delay can be adjusted to meet the conditions of beamsteering in any desired angle. Fig. 1c shows the location of the feedpoint a to direct the beam in the direction of $-\alpha$ from the undeflected position. Therefore, a system can be built to combine the concept shown in Fig. 1a, 1b, and 1c to realize a compact beamforming and beamsteering system as shown in Fig. 1d. In this case, the system will have 3 feed positions or beamports and 3 or more receiving positions also called array ports. The beamports can be excited sequentially or simultaneously by single pole multi throw switches. Obviously, the lens can have any number of beamports and array ports as long as the condition of beamforming is satisfied.

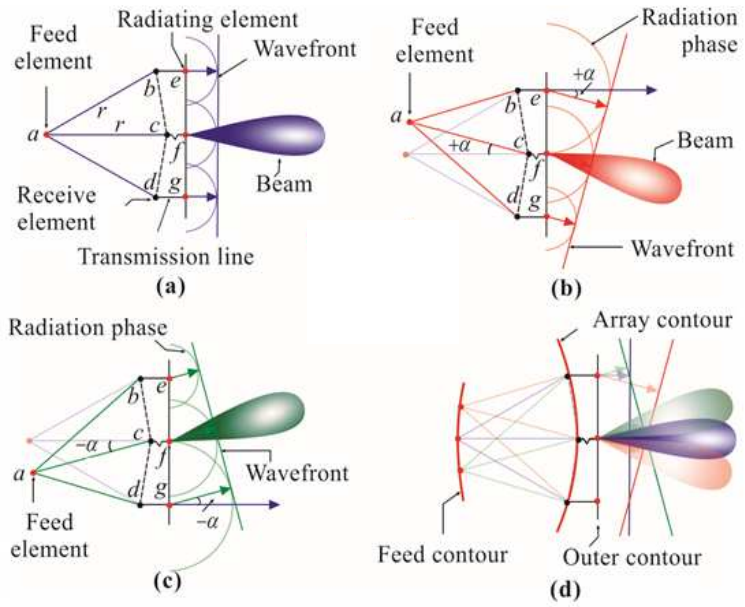

Fig. 1. A qualitative description of lens operation.

There are some reflection form the upper and bottom side walls between the feed contour and the array contour. To minimize the reflection, dummy ports are used to absorb RF power to minimize sidewall reflection. This lens geometry was first proposed by Rotman and Turner. The details of design procedure are well explained in [2, 10, 11]. In standard Rotman lens [2], the length of array transmission lines is an important factor to determine the location of the array ports for proper beamforming. Array port coordinate $P(x, y)$, Fig. 2, can be calculated from equations (1) and (2) [2]

$$y = \frac{b_1}{b_0} n \left(\frac{1}{\sqrt{\varepsilon_r}} - \frac{\sqrt{\varepsilon_{eff}}}{\varepsilon_r} \omega \right) \tag{1}$$

$$x^2 + y^2 + 2gx = \frac{\varepsilon_{eff}}{\varepsilon_r} \omega^2 - 2 \frac{\sqrt{\varepsilon_{eff}}}{\sqrt{\varepsilon_r}} g\omega \tag{2}$$

Where the length of the delay line (ω) can be verified using equations (3-6)

$$a\omega^2 + b\omega + c = 0 \tag{3}$$

where

$$a = \frac{\varepsilon_{eff}}{\varepsilon_r}\left(1 - \frac{1}{\varepsilon_r}\left(\frac{b_1}{b_0}\right)^2 n^2 - \left(\frac{g-1}{g-a_0}\right)^2\right) \tag{4}$$

$$b = \sqrt{\frac{\varepsilon_{eff}}{\varepsilon_r}}\left(2g\left(\frac{g-1}{g-a_0}\right) - \frac{1}{\varepsilon_r}\left(\frac{g-1}{(g-a_0)^2}\right) b_1^2 n^2 + \frac{2}{\varepsilon_r}\left(\frac{b_1}{b_0}\right)^2 n^2 - 2g\right) \tag{5}$$

$$c = \frac{1}{\varepsilon_r}\left(\frac{g b^2 n^2}{g-a_0} - \frac{b^4 n^4}{4\varepsilon_r (g-a_0)^2} - \left(\frac{b_1}{b_0}\right)^2 n\right) \tag{6}$$

where $= N/F, \omega = (W - W_0)/F,$ $x = X/F$, $y = Y/F$, $g = G/F$ also $a_0 = \cos\alpha,\ b_0 = \sin\alpha, a_1 = \cos\varphi, b_1 = \sin\varphi$. The length of the true time delay line (ω) and the array port coordinates $P(x, y)$ can be determined by designer from design parameters of axis focal length (G), off axis focal length (F), total element spacing (N), focal angle (α), scanning angle (φ), the ratio of on-axis to off-axis focal length (g), the dielectric constant of the substrate at design frequency(ε_r), and the effective dielectric constant of the delay line (ε_{eff}).

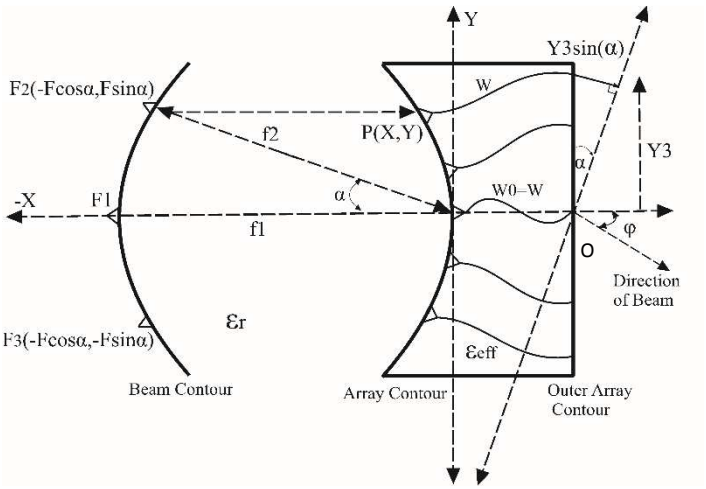

Fig. 2. Scheme of the lens design.

III. PROPOSED ROTMAN LENS DESIGN METHODOLOGY

A new Rotman lens design technique, in which the progressive phase delay is realized independent of array transmission lines length, has been developed in this work. This methodology reduces the number of design variable while improving phase error.

Path length error determines the phase error of Rotman lens [2]. Considering Fig. 2, in conventional Rotman lens the path length error, ΔL_c, is determined from (7)

$$\Delta L_c = \left|\overrightarrow{F_2P}\right| + |W| + |Y_3 \sin\alpha| - \left|\overrightarrow{F_2O}\right| - |W0| \quad (7)$$

In which $|W| - |W0| > 0$. In the proposed design, equal taper and array transmission line length have been chosen and therefore $|W| = |W0|$. In this case the path length, ΔL_p, can be calculated from (8)

$$\Delta L_p = \left|\overrightarrow{F_2P}\right| + |Y_3 \sin\alpha| - \left|\overrightarrow{F_2O}\right| \quad (8)$$

It can be seen from (7) and (8) that $\Delta L_c > \Delta L_p$ for $|W| - |W0| > 0$ which indicates that the proposed method supports better phase error performance if $|W| > |W0|$.

Reducing the size of focal length (f_1 =2λ) can further improve the phase error performance. This would also help to reduce the physical size of the lens. There is a trade-off between scanning angle and phase error, as scanning angle rises the phase error increases. A Gaussian optimization process has been conducted to sustain wide scanning angle while supporting low sidelobes level and phase error. For example, higher contour curvature and medium routed array transmission line could provide lower sidelobe level.

Using ray optic theory [12] and assuming the length of all transmission lines are equal W=W_0, the ray optic equations can be written as follow

$$\overrightarrow{F_2P} + Y_3 \sin\alpha = f_2 \tag{9}$$

$$\overrightarrow{F_1P} = f_1 \tag{10}$$

$$\overrightarrow{F_3P} - Y_3 \sin\alpha = f_2 \tag{11}$$

While the length of each path can be calculated as follows

$$\left|\overrightarrow{F_2P}\right|^2 = (-f_2 \cos\alpha - X)^2 + (-f_2 \sin\alpha + Y)^2 \tag{12}$$

$$\left|\overrightarrow{F_1P}\right|^2 = (f_1 - X)^2 + Y^2 \tag{13}$$

$$\left|\overrightarrow{F_3P}\right|^2 = (-f_2 \cos\alpha - X)^2 + (f_2 \sin\alpha + Y)^2 \tag{14}$$

After normalizing all the equations (9-14) and mathematical simplifications, location of each array port on the array contour can be calculated from equations (15, 16).

$$x = \frac{[(Y_3/f_1)sin\alpha]^2}{2[1+(f_2/f_1)cos\alpha]} \tag{15}$$

$$y = \frac{Y_3}{f_1} \tag{16}$$

Considering the focal length and the path-length error, the overall size and geometry of the lens can be minimized. Detailed procedure to determine the initial beams location following the ray optics theory is available in [2, 12].

IV. MICROSTRIP LENS DESIGN ON LTCC

A Rotman lens operating at 60GHz is designed based on the method presented in section III to validate the proposed method. The microstrip Rotman Lens has been designed for

millimeter-wave band at the center frequency of 60 GHz for RFID applications. Number of beam ports has been chosen to be five to have wide range of steering beam with small amount of phase error.

To support wide scanning capability, a scan angle of 30^o has been chosen to cover an azimuthal angle of 60^o at -6 dB of antenna radiation pattern. The antenna beam pattern is chosen to be approximately 15^o at -3dB to have a beam overlap. The array element spacing along the outer contour has been initially chosen to be $0.5\lambda_0$. Element spacing helps to determine the microstrip patch antenna row spacing to obtain the desired beamwidth. This leads to length of 5 mm for Y3 as shown in Fig. 2.

To keep the geometry compact, the scan angle φ has been selected to be the same as the focal angle α. To implementation the structure, LTCC substrate has been chosen which has a very low loss tangent and absorption coefficient. The low line losses as well as the competitive manufacturing costs are the main advantages of LTCC for RF and microwave applications.

After initial design specifications were set, the lens geometry was simulated with 3D FDTD simulator and the results were confirmed with Finite Element Method (FEM) analysis. The design parameters including geometric dimensions and losses were then optimized using sidelobe levels, phase errors, and sidewall curvature as cost functions. To support the quasi-TEM condition the maximum allowed substrate thickness can be determine from (17) [13, 14].

$$f_t = \frac{150}{\pi h}\sqrt{\frac{2}{\varepsilon_r - 1}}\tan^{-1}\varepsilon_r \quad (17)$$

where f_t and h are cut off frequency in gigahertz and thickness in millimeter, respectively.

As for the metal, a 10 μm thick gold layer with conductivity 4.1x10^7 S/m has been selected instead of copper to avoid any degradation of performance due to copper oxidation in real word deployment. To optimize the beam to array coupling, beam pointing technique has been used. The width of the microstrip taper for the beam and the array ports is set to $\lambda/2$ to prevent coupling of second order mode. The length and shape of microstrip taper allows adjusting the flare angles of the ports to achieve acceptable performance such as lower sidelobes and better reflection coefficient and voltage standing wave ratio (VSWR). To minimize the spillover loss from sidewall reflection, terminated dummy ports are used. To reduce the size and lower the cost of fabrication the number of dummy ports is reduced to two at each side of the lens. The widths of the dummy ports are also determined to be $\lambda/2$ to lower the sidelobe levels [15]. Simulation results using 3D FDTD simulator show that low curvature lens sidewalls have much higher sidelobes though the main beam levels or width are not affected by sidewall curvature. However, excessive curvature also increases the lens size. Thus an optimum value of sidewall curvature was determined. A cross-sectional geometry of the lens is shown in Fig. 3a and the top view of the optimized lens geometry is shown in Fig. 3b.

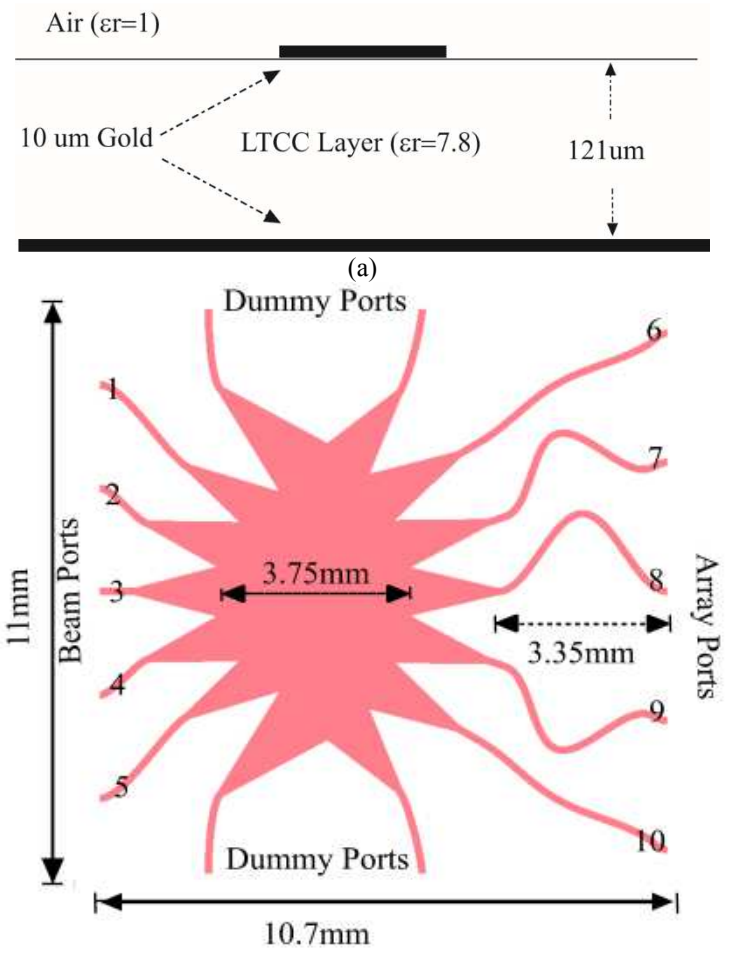

Fig. 3. Rotman lens geometry. (a) cross section. (b) top view

V. SIMULATION RESULTS

The main parameter for Rotman Lens is its array factor which presents beam direction, angle and level of sidelobes. Beam pattern is calculated from FDTD S-parameters simulator results [12] using (18).

$$AF = \cos\alpha * \left|\sum_{n=1}^{N} e^{ik_0(n-1)dsin\alpha} e^{ikW_n} S_{mn}\right|^2 \quad (18)$$

Where α, N, k_0, k, d, W_n are scan angle, number of array ports, wave number of free space and constrained lines, element spacing and the length of nth restricted line antenna, respectively. The array factor is shown in Fig. 4 for different beamports excitation which has sidelobes of less than -12dB. Array factor analyses indicate medium beam transmission lines and routed medium array transmission lines with smaller tapers flare angle are the best choice to lower the sidelobes level. Array factor analyses exhibit higher lens curvature, flare angle with medium size of routed transmission lines provide lower sidelobes and better performance.

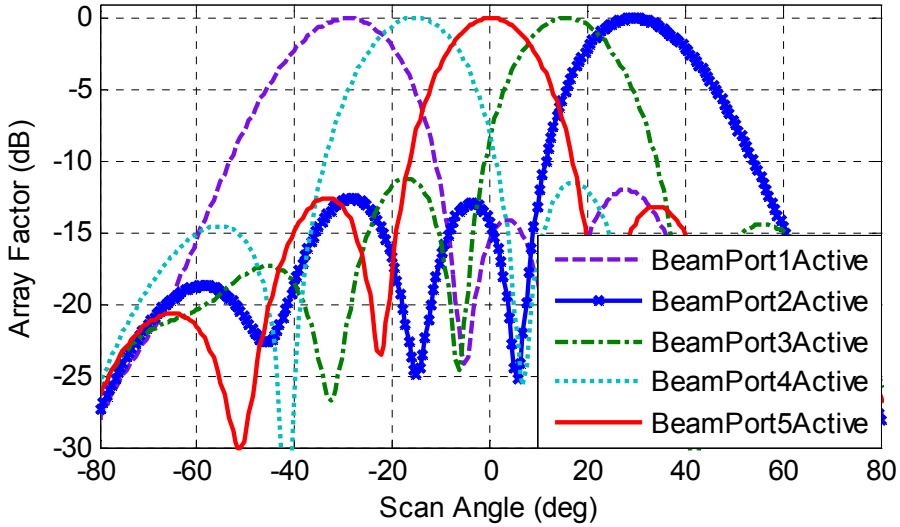

Fig. 4. Synthesized Array factor for beam ports

The other important factor is accuracy in the steering and the maximum phase error associated with different beamports excitation. Phase error can be determined by comparing electrical lengths along two different paths from a given beam port through the lens [2]. The first path travels along each of the off axis array ports. As for the second path,

it begins at the same beam port but travels through the center of the array curve. Fig. 5a shows the layout of the proposed and a sample of conventional Rotman lens. Beam to array phase error for all ports of the proposed scheme is shown in Fig. 5b.

It can be seen that the maximum beam to array phase error for all beam ports fall below 0.45˚. Fig. 5c shows the average phase error of all beam ports through array ports for the conventional and the proposed Rotman Lens schemes. The average phase error of the proposed Rotman lens falls below 0.25˚ which is a considerable improvement compared to 0.42˚ for the conventional approach.

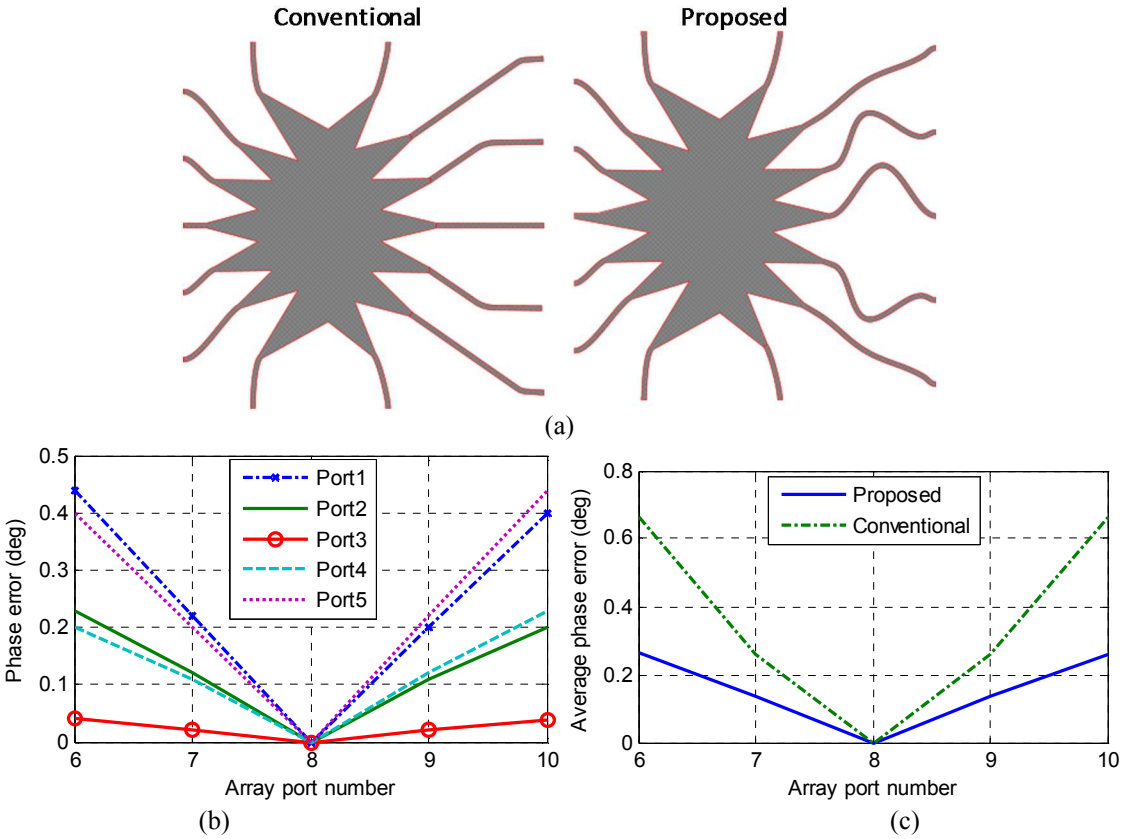

Fig. 5. Beam to array phase error (a) for different beam port (b) top view of proposed and conventional geometry(c) average phase error of all beam ports for proposed and conventional transmission lines.

Fig. 6 presents the return loss for beam port number 1 to 5 which it is arising from discontinuity in a transmission line.

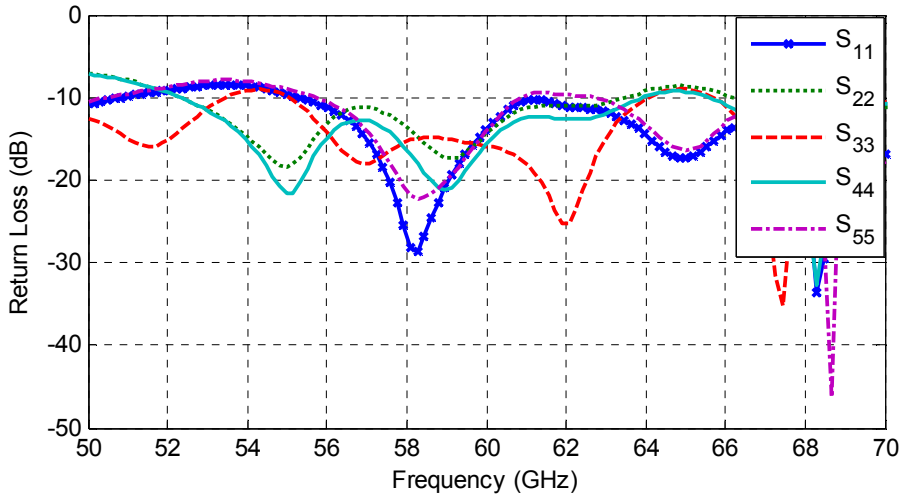

Fig. 6. Return loss(dB) over different frequency.

Insertion loss arises from the insertion of the lens in the transmission lines. The insertion loss of the Rotman lens is determined by adding the received powers at the array ports for each individual beam ports. The insertion loss of a Rotman lens can also be calculated from division of the array ports power to each individual beam port or summation of S-parameters using (19)

$$Insertion\ Loss_k = -10log\sum_n |S_{nk}|^2 \tag{19}$$

where k is number of beam ports and n is number of array ports.

The insertion loss for all beam ports over wide range of frequency is shown in the Fig. 7. The average insertion loss of all beam ports is less than 2.2dB at the center frequency of 60 GHz.

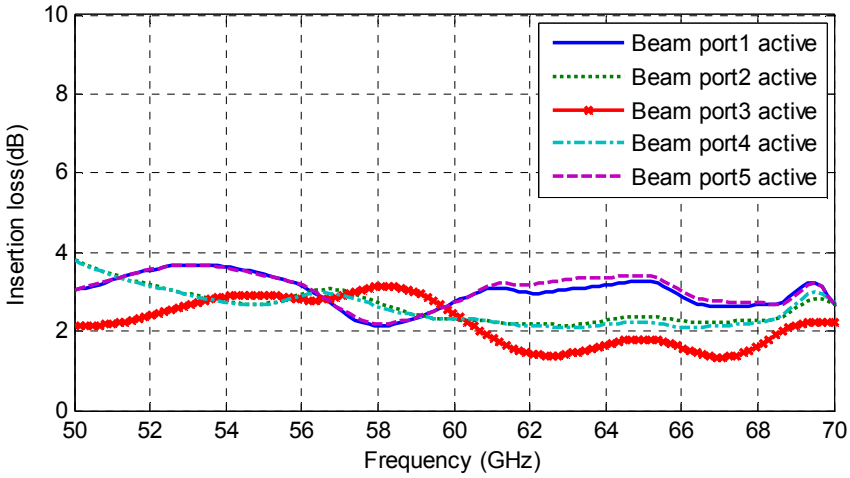

Fig. 7. Insertion loss for all beam ports.

Crosstalk is caused by unwanted coupling of energy between two or more adjacent transmission lines which can produce undesired effects on signal lines. The amount of coupling between adjacent ports of Rotman lens can be determined from S-parameters. For instance, S_{21} can be used to calculate the amount of coupling between beam ports number one and two, Fig. 8.

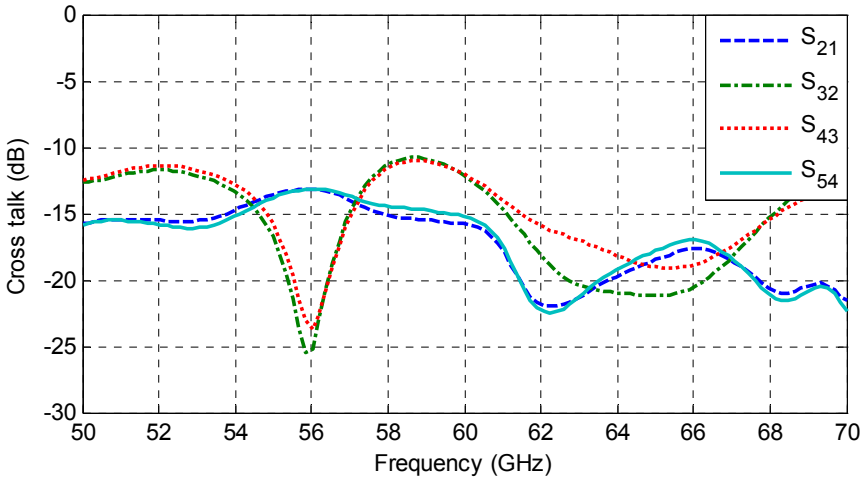

Fig. 8. Crosstalk for all beam ports.

The electric field simulation of current propagating across the lens for beam port number three is shown in Fig. 9. It can be seen that much of the wave energy propagates through the array ports and only a small fraction of the wave energy reaches the dummy Ports. Interaction between the sidewalls and the radiation from beam port number one and five are more significant than the center beam. Table I lists the key performance parameters of the designed Rotman lens and state-of-the-art 60GHz Rotman lenses in the literature.

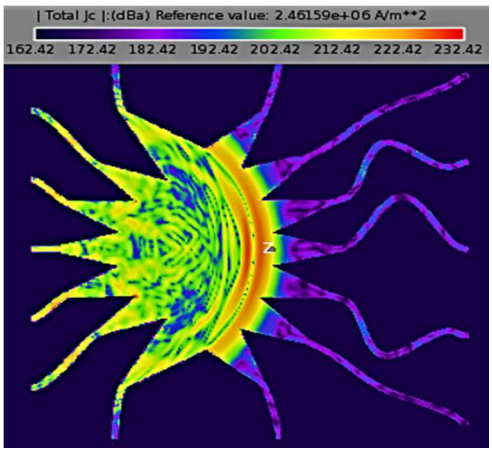

Fig. 9. Current propagating across the lens for beam port number three active.

TABLE I
Comparison of key features

Parameter	Ref. [16]	Ref. [1]	This paper
Frequency (GHz)	60	60	60
Material	LTCC (εr=7.05)	Silicon&Sio2 (εr=11.7&3.9)	LTCC (εr=Green7.8/Fired7.1)
Thickness(μm)	***	300&1.5	Green121/Fired112
Length×Width(mm)	21×10	19.6×20	11×10.7
No. of beamports	3	5	5
No. of array ports	5	7	5
Scan Angle (deg.)	25	30	30
Phase error(deg.)	7	6	0.45
Insertion loss (dB)	3.1	***	2.2
Return loss (dB)	***	-6dB	-12dB

V. MICROWAVE BEAMFORMER AND INSET FED MICROSTRIP PATCH ANTENNA

Microstrip patch antenna is a highly desirable choice in integrated packaging system due to low cost, ease of fabrication and simple structure. To support high gain and directivity a microstrip patch array is used in this work. The antenna is designed on 121μm LTCC substrate with 7.8 dielectric constant and 0.001 loss tangent. Fig. 10a shows detailed dimensions of the implemented inset fed microstrip patch array antenna. To feed the antenna a 50 ohm $\lambda/2$ transmission line is applied. Fig. 10b exhibits the full 3D gain pattern of the microwave lens connected to the microstrip patch antenna array. Fig. 10c and d display gain pattern for azimuthal angle, Φ, equal to 0^o and 90^o with scanning angle of θ equal to 360^o, respectively. In Fig. 10c, the difference between main lobe and highest side lobe is 14dB.

VI. CONCLUSION

This work presents a new design methodology for implementation of an optimized microwave Rotman lens. The proposed method reduces the design complexity of Rotman lens and enhances its performance parameters. A Rotman lens together with an array antenna was implemented and simulated using the proposed method. The implemented lens exhibits a good insertion loss, return loss, and shows phase error as small as 0.45^o in the worst-case. The lens was designed on a 121μm thick LTCC with total scanning angle of 60^o in 5 steering steps. The lens is capable of steering the beam by $\pm 15^o$ from the undeflected position. Full wave simulation results indicate that the side lobe level falls

below -12dB with the half power beamwidth of 30º. Array factor analyses exhibit higher lens curvature, flare angle with medium size of routed transmission lines provide lower side lobs and better performance.

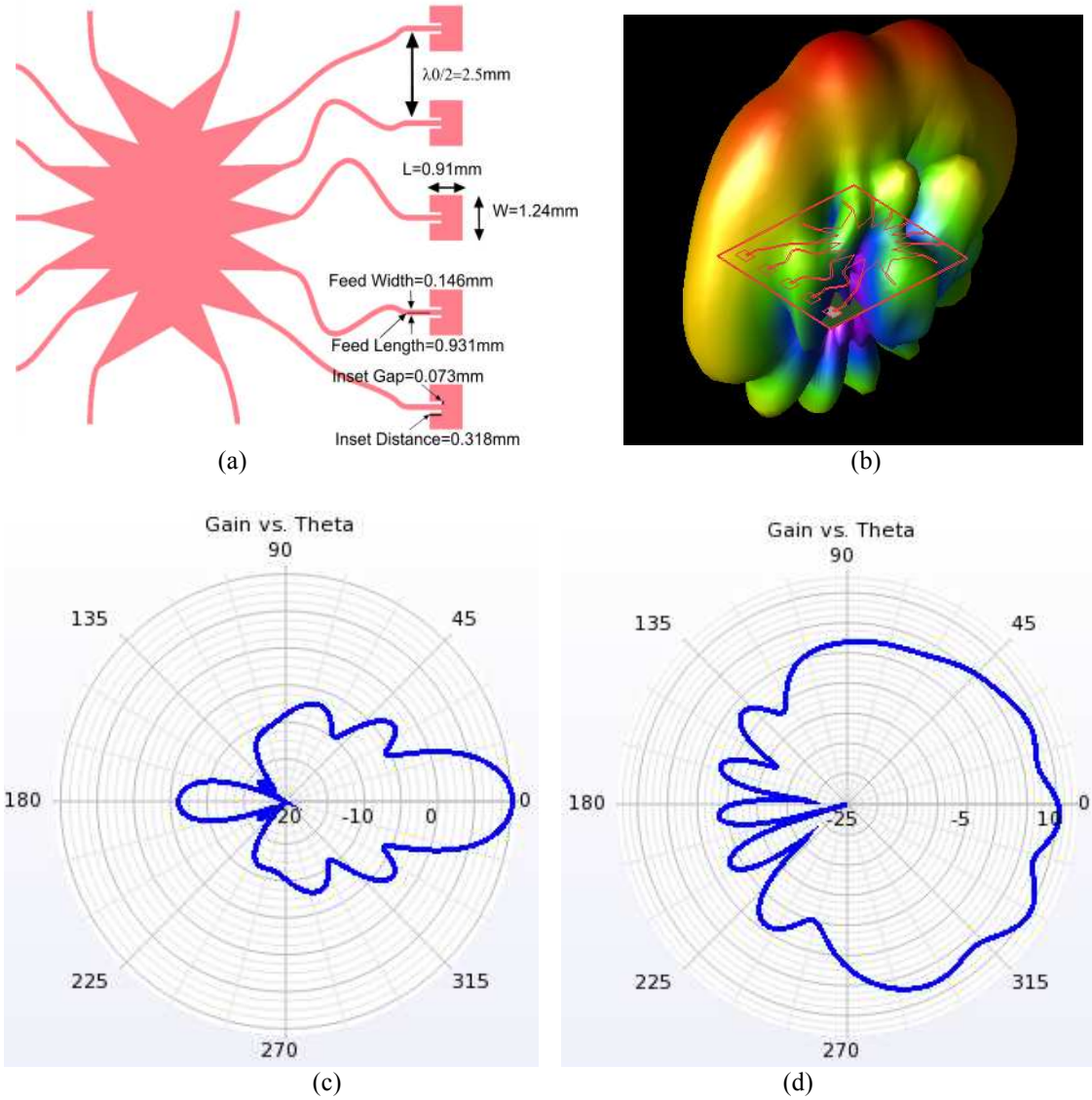

Fig. 10. (a) Microwave lens connected to microstrip patch antenna, (b) Full 3D gain pattern, (c) Gain vs. theta for phi=90º and (d) Gain vs. theta for phi=0º

REFERENCES

[1] Lee W, Kim J, Cho CS, and Yoon Y J, 'A 60 GHz Rotman lens on a silicon wafer for system-on-a-chip and system-in-package application', in IMS. IEEE Conf., September 2009, pp. 1189-1192.

[2] Rotman W, and Turner R F, 'Wide-angle microwave lens for line source applications', IEEE Trans. Antennas Propag., 1963, 11, (6), pp. 623-632.

[3] Lambrecht A, Beer S, and Zwick T, 'True-time-delay beamforming with a Rotman-lens for ultrawideband antenna systems', IEEE Trans. Antennas Propag., 2010, 58, (10), pp. 3189-3195.

[4] Pursula P, Karttaavi T, Kantanen M, Lamminen A, Holmberg J, Lahdes M, Marttila I, Lahti M, Luukanen A, and Vähä-Heikkilä T, '60-GHz millimeter-wave identification reader on 90-nm CMOS and LTCC,' IEEE Tran. on Microwave Theory and Techniques, 2011, 59, (4), pp.1166-1173

[5] Pursula P, Vähä-Heikkilä T, Müller A, Neculoiu D, Konstantinidis G, Oja A, and Tuovinen J, 'Millimeter-wave identification—a new short-range radio system for low-power high data-rate applications', IEEE Tran. on Microwave Theory and Techniques, 2008, 56, (10), pp.2221-2228.

[6] Hall LT, 'Broadband monolithic constrained lens design', Ph.D. thesis, The University of Adelaide, 2009.

[7] Lee W, Kim J, and Yoon YJ, 'Compact two-layer Rotman lens-fed microstrip antenna array at 24 GHz', IEEE Trans. Antennas Propag., 2011, 59, (2), pp. 460-465.

[8] Mailloux RJ, 'Phased array antenna handbook'. Boston, MA: Artech House, 1994.

[9] Ruze J, 'Wide angle metal plate optics', Proc. IRE, 1950, 38, (1), pp. 53-59.

[10] Katagi T, 'An improved design method of Rotman lens antennas', IEEE Trans. Antennas Propag., 1984, 32, (5), pp. 524-527.

[11] Musa L, and Smith M, 'Microstrip Rotman lens port design', Antennas and Propagation Society International Symposium, June 1986, 24, pp. 899-902.

[12] Dong J, 'Microwave lens design: optimization, fast simulation algorithms, and 360-degree Scanning techniques', Ph.D. thesis, the Virginia Polytechnic Institute and State University, 2009.

[13] Gupta KC, Garg, R., Bahl, I., and Bhartia, P.: Microstrip lines and slotlines. Norwood, MA: Artech House, 1996.

[14] Lee W, Kim J, Cho CS, and Yoon YJ, 'Beamforming lens antenna on high resistivity silicon wafer for 60 GHz WPAN', IEEE Trans. Antennas Propag., 2010, 58, (3), pp. 706-713.

[15] Kim J, and Barnes FS, 'Scaling and focusing of the Rotman lens', IEEE AP-S Int. Symp. Dig., July 2001, pp. 773-776.

[16] Song IS, Kim J, Jung DY, Eun KC, Lee JJ, Cho SJ, Kim HY, Bang JH, Oh IY, and Park CS, '60GHz Rotman lens and new compact low loss delay line using LTCC technology', RWS Symposium IEEE, January 2009, pp. 663-666.

Chapter 5

A 60-GHz Radio Frequency Identification Reader Using Passive Mixer

Millimeter wave identification (MMID) system for low power, high data rate and short range wireless communication systems has been investigated [1-2] by many researchers. 60 GHz RFID reader can be realized for military and commercial applications such as next generation of WPAN/LAN, intelligent highway and human implant [1-2].

To reduce the complexity and consequently the size of 60 GHz RFID readers a 180° hybrid coupler can be utilized. In this configuration the Tx and Rx signals become 180° out of phase to avoid interference between them. A microwave passive mixer combined with a ring hybrid coupler up convert the outgoing signal and the incoming signal is down converted for the purpose of communication.

A 79 GHz radar transceiver with switchable T_X and Local Oscillator (LO) feed-through in a Silicon-Germanium technology is presented in [3]. T_X and R_X paths are separated using a Rat-Race coupler. A low power micro-mixer with high linearity in silicon-Germanium bipolar technology using directional coupler and Gilbert mixer is proposed in [4] for automotive radar applications at center frequency of 77 GHz. In this monostatic radar system, a directional coupler is utilized to send and receive the signal through an antenna. In [5] a 76 to 77 GHz GMIC mixer for automotive radar is developed to provide a fully passive front-end. Low cost and wideband mixer for the 10.7 GHz to 12.8 GHz direct broadcast satellite market using rat-race mixer is presented in [6]. A 60 GHz MMID reader on 90 nm CMOS and LTCC substrate using power divider is developed in [1].

In this brief, a low cost mixer is realized using a flip-chip dual GaAs diode. The proposed reader architecture can send and receive signal using 180° ring hybrid coupler. Simulations were carried out on a LTCC substrate using Agilent 3-D software (ADS, Genesys and Empro). 3-D full wave simulations were conducted to achieve accurate results. The 3D simulation environment was also used to optimize the geometry of the coupler and microwave mixer.

II. PROPOSED READER STRUCTURE

A UHF RFID reader can be implemented based on the direct conversion architecture. Using the principle of operation for frequency modulated continuous wave (FMCW) radar, the MMID reader can be enabled to detect the reflected signal from the tag with some time

delays. An example of direct conversion FMCW MMID reader is presented in [1]. The module is realized using multilayer LTCC and flip chip CMOS components. Antenna arrays, filters, power dividers, and other passives elements are fabricated using the LTCC substrate. The components are connected to a printed circuit board (PCB) with a ball grid array (BGA) [1].

In [7], a direct conversion FMCW radar module at center frequency of 77 GHz is illustrated using SiGe technology and external antennas. In radar a phase locked loop (PLL) is required for frequency sweep [1, 8, 9]. However, in MMID reader there is no need for a PLL as the LO frequency is not swept.

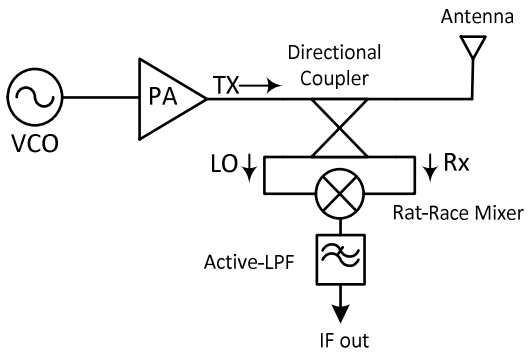

Fig 1. Block diagram of the MMID reader

A direct conversion architecture using 180° ring hybrid coupler is selected for the proposed MMID reader, Fig 1. The Voltage controlled oscillator (VCO) generates a 60GHz signal which is amplified by the power amplifier (PA). Half of the signal is sent to the antenna with 180° out of phase and the other half to the LO port of the mixer for down conversion of signals received from tag. This architecture can provide sufficient sensitivity

and output power with low power consumption. In this approach the minimum number of element is used to reduce the size. It also supports a wide bandwidth and high data throughput due to the employed high bandwidth coupler.

III. POWER MAPPING

The read range and the estimated required power for each element to send and receive signals are calculated in this part. Received power at the input of the reader at distance R from MMID tag can be calculated from equation (1) [10],

$$P_r = \frac{P_t \,.G_t \,.G_r \,.\sigma \,.\lambda^2}{(4\pi)^3 \,.\, R^4} \tag{1}$$

where $\lambda = \frac{c}{f\sqrt{\varepsilon_r}}$ is realized using LTCC substrate. P_r is the received power at the input of antenna considering free space path loss, P_t is the transmitted power from MMID reader, G_t is the gain of antenna in the transmit link or downlink, G_r is the gain of antenna in the received link or uplink, σ is the tag cross section which can be determined from $\sigma = \lim_{r\to\infty} 4\pi r^2 \times \frac{S_S}{S_i}$. Where S_S is the scattered power density seen at distance R from target and S_i is incident power density measured at the target. Limiting factors on the passive MMID range at 60 GHz lead to tag cross section of equal to almost one $\sigma = \frac{G_A^2.\lambda^2}{4\pi} m$ [1]. Where G_A=20dB is the tag antenna array gain and $m = |\Gamma_1 - \Gamma_2|^2/4$ is the modulation coefficient. Considering limiting factors on the passive MMID range at 60 GHz, modulation coefficient can be obtained from $m = \frac{|\Gamma_1 - \Gamma_2|^2}{4} = \frac{3.24}{4} = 0.81$ [3].

Minimum detectable power which receiver is able to detect can be determined from

$$P_{RXmin} = P_N + NF_{total} + 10log\, BW_{FFT} + SNR_{min} \quad (2)$$

where P_N=KTB=-174 dBm, as k=1.38x10^{-23} is Boltzman's constant, T=270 k and B=1 Hz. Using Frii's formula for total noise factor of a cascade receiver,

$$F = F_1 + \frac{F_2-1}{G_1} + \frac{F_3-1}{G_1.G_2} + \frac{F_4-1}{G_1.G_2.G_3} .... \quad (3)$$

where gain and noise factor of each element represented with G and F, respectively.

To calculating FFT resolution bandwidth (BW_{FFT}), the sampling frequency should divided by the size of FFT. Detection threshold or SNR_{min} which shows minimum required signal to noise ratio for signal processing for 99% detection, is equal to 16 dB [10]. For proper signal detection the power of the received signal should be higher than the minimum level ($P_r > P_{RXmin}$).

To ensure that the radiation power of the antenna exceeds the required power in equation (1) either the VCO output power or the gain power amplifier can be increased.

IV. 180° RING HYBRID COUPLER

Couplers are passive microwave components used for power division or combining [11]. A coupler is a four-port component, with or without loss. Directional couplers can be designed for arbitrary power division, while hybrid junctions usually have equal power division. Hybrid junctions commonly have either a 90° or a 180° shift between the outer

ports. There are different types of coupler such as waveguide directional couplers. Single hole waveguide has a narrow bandwidth so to have wide bandwidth instead of a single hole a series of holes should be used. Quadrature hybrids are 3dB directional couplers with 90° phase difference in the outputs of the through and coupled arms. This type of hybrid couplers is often made of microstrip or stripline.

When two unshielded transmission lines are close together, power is coupled between the lines such an arrangement represents a coupled line directional coupler which operates in the TEM mode [11]. Generally the coupling in a coupled line coupler is not enough to achieve coupling factors of 3 dB or 6 dB. One way to increase the coupling between the edge-coupled lines is to use several lines parallel to each other, so that the fringing fields at both edges of a line contribute to the coupling. With 4 coupling line, this coupler can easily achieve 3 dB coupling ratios, with an octave or more bandwidth. The main disadvantage of this coupler also called Lange coupler is the implementation. The lines are required to be very narrow and close to each other. These requirements make it difficult to fabricate the necessary bonding wires across the lines [11]. The 180° hybrid junction is a four-port network with a 180° phase shift between the two output ports. In addition, it can add in-phase outputs with proper inputs excitation. It can work as a combiner if the input signals are applied to the ports 2 and 3 and the output which is the sum of the inputs is observed at port 1. It has simple structure so fabrication process is easy [11]. Fig. 2 shows a 180° hybrid junction coupler.

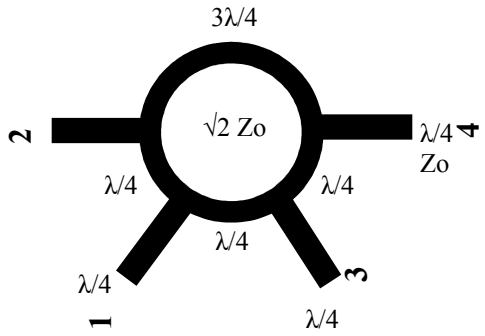

Fig 2. 180° hybrid junction couple6r

The ring hybrid coupler can have a negative output (1,-1). To characterize the hybrid ring coupler, the scattering parameters are calculated. As there are four ports, scattering matrix should be 4x4.

$$[S] = \begin{bmatrix} S_{11} & S_{12} & S_{13} & S_{14} \\ S_{21} & S_{22} & S_{23} & S_{24} \\ S_{31} & S_{32} & S_{33} & S_{34} \\ S_{41} & S_{42} & S_{43} & S_{44} \end{bmatrix} \tag{4}$$

Due to symmetry $S_{11}=S_{33}$, $S_{22}=S_{44}$, and $S_{21}=S_{43}$ and from reciprocity $S_{12}=S_{21}$ and $S_{34}=S_{43}=S_{21}$. If port 1 is excited the signal transmits to port four (S_{41}) and by symmetry $S_{41}=S_{23}$. There is a transmission between S_{31} which by reciprocity $S_{31}=S_{13}$, and also $S_{41}=S_{14}$, $S_{32}=S_{41}$. In the [S] matrix, there are 6 variables that should be determined.

Exciting port 1 with a unit wave ($a_1=1$) allows calculation of four variables as $S_{11}=b_1/a_1$, $S_{21}=b_2/a_1$, $S_{31}=b_3/a_1$ and $S_{41}=b_4/a_1$. To obtain the two other remaining parameters, S_{22} and

S_{24}, either port 2 (a_2=1) can be excited or unitary property can be applied for assumed lossless network.

$$[S] = \begin{bmatrix} S_{11} & S_{21} & S_{31} & S_{41} \\ S_{21} & S_{22} & S_{41} & S_{24} \\ S_{31} & S_{41} & S_{11} & S_{21} \\ S_{41} & S_{24} & S_{21} & S_{22} \end{bmatrix} \tag{5}$$

Even and odd mode analyses by redrawing the symmetry lines, Fig. 3, equations can be simplified and by just calculation for half of the circuit, the desire variables can are obtained from $b_1 = \frac{1}{2}(b_{1E} + b_{1O})$, $b_2 = \frac{1}{2}(b_{2E} + b_{2O})$, $b_3 = \frac{1}{2}(b_{3E} + b_{3O})$ where $b_3 = \frac{1}{2}(b_{1E} + b_{1O})$ and $b_4 = \frac{1}{2}(b_{2E} - b_{2O})$.

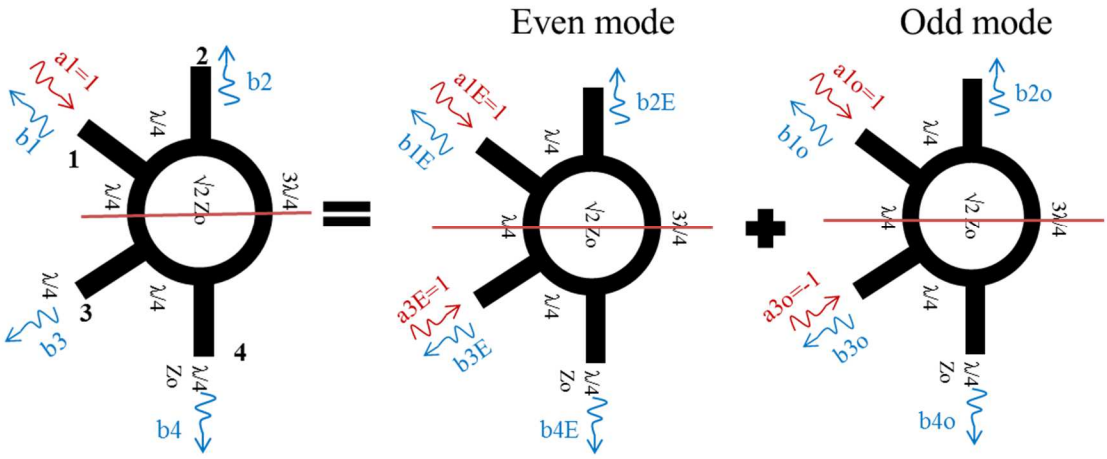

Fig. 3 Even and odd mode symmetry lines

Transmission line theory is used again to obtain even mode and S-parameters using cascade ABCD method, Fig. 4.

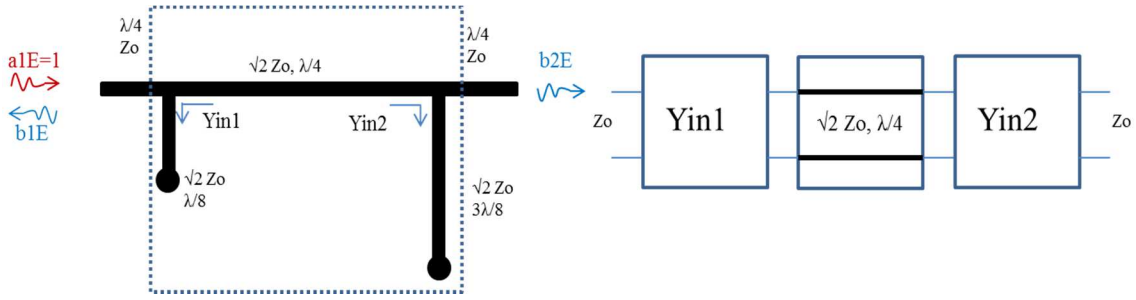

(a) (b)

Fig. 4 (a) Transmission line analysis for even mode between port one and two, (b) Equivalent circuit

In the even mode λ/8 and 3λ/8 stubs are open circuit. For an open circuit transmission line Y_{in1} and Y_{in2} are calculated as follow: $Y_{in1} = j\frac{Y_0}{\sqrt{2}}\tan\beta l = j\frac{Y_0}{\sqrt{2}}\tan\frac{2\pi}{\lambda}.\frac{\lambda}{8} = j\frac{Y_0}{\sqrt{2}}$ and $Y_{in2} = -j\frac{Y_0}{\sqrt{2}}$. This follow by using the cascade ABCD method [9-10] to determine the S-parameters, equation (6-8):

$$\begin{bmatrix} A & B \\ C & D \end{bmatrix}_E = \begin{bmatrix} 1 & 0 \\ j\frac{Y_0}{\sqrt{2}} & 1 \end{bmatrix} \cdot \begin{bmatrix} 0 & j\sqrt{2}Z_0 \\ j\frac{Y_0}{\sqrt{2}} & 0 \end{bmatrix} \cdot \begin{bmatrix} 1 & 0 \\ -j\frac{Y_0}{\sqrt{2}} & 1 \end{bmatrix} = \begin{bmatrix} 1 & j\sqrt{2}Z_0 \\ j\frac{2Y_0}{\sqrt{2}} & -1 \end{bmatrix} \quad (6)$$

where $b_{1E} = \frac{A+B/Z_0 - CZ_0 - D}{A+B/Z_0 + CZ_0 + D} = \frac{-j}{\sqrt{2}}$ and $b_{2E} = \frac{2}{A+B/Z_0 + CZ_0 + D} = \frac{-j}{\sqrt{2}}$.

Using conversion formula and rewriting transmission line equations for odd mode considering grounded λ/8 and 3λ/8, $b_{1O} = \frac{A+B/Z_0 - CZ_0 - D}{A+B/Z_0 + CZ_0 + D} = \frac{j}{\sqrt{2}}$ and $b_{2O} = \frac{2}{A+B/Z_0 + CZ_0 + D} = \frac{-j}{\sqrt{2}}$ are obtained.

Substituting for the obtained variable into S-parameter equations which mentioned earlier, four of the desire parameters are determined.

$$S_{11} = b_1 = \frac{1}{2}(b_{1E} + b_{1O}) = \frac{1}{2}\left(\frac{-j}{\sqrt{2}} + \frac{j}{\sqrt{2}}\right) = 0 \quad (7)$$

$$S_{21} = b_2 = \frac{1}{2}(b_{2E} + b_{2O}) = \frac{1}{2}\left(\frac{-j}{\sqrt{2}} + \frac{-j}{\sqrt{2}}\right) = \frac{-j}{\sqrt{2}} \quad (8)$$

$$S_{31} = b_3 = \frac{1}{2}(b_{1E} + b_{1O}) = \frac{1}{2}\left(\frac{-j}{\sqrt{2}} + \frac{-j}{\sqrt{2}}\right) = \frac{-j}{\sqrt{2}} \quad (9)$$

$$S_{41} = b_4 = \frac{1}{2}(b_{2E} - b_{2O}) = \frac{1}{2}\left(\frac{-j}{\sqrt{2}} - \frac{-j}{\sqrt{2}}\right) = \frac{-j}{\sqrt{2}} \quad (10)$$

By exciting port two and using the even and odd mode analysis, S_{22} and S_{24} can be calculated.

$$S_{22} = 0 \quad (11)$$

$$S_{24} = \frac{j}{\sqrt{2}} \quad (12)$$

Therefore, final scattering matrix is obtained, equation 13. It also shows negative derivation due to port 2 or port4 excitation.

$$[\mathrm{s}] = \frac{-\mathrm{j}}{\sqrt{2}}\begin{bmatrix} 0 & 1 & 1 & 0 \\ 1 & 0 & 0 & -1 \\ 1 & 0 & 0 & 1 \\ 0 & -1 & 1 & 0 \end{bmatrix} \quad (13)$$

After initial geometry design of the coupler at 60GHz center frequency on 121 um LTCC, 3-D full wave electromagnetic analysis tools, ADS and Genesys, was used to conduct the simulations. The results are shown in Fig. 5. Port 2 s-parameters indicate that the signal is equally divided between port 1 and port 4 and no signal passes through port 3.

II. MICROWAVE PASSIVE MIXER

Mixers are commonly three port active or passive devices which used to mix signal to up-convert or down-convert signals. The mixing can be performed in two ways, switching and

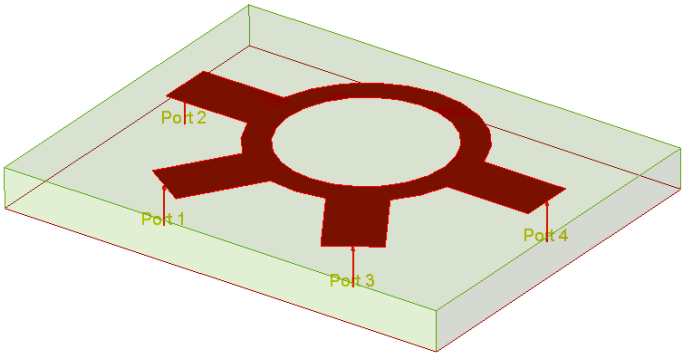

(a)

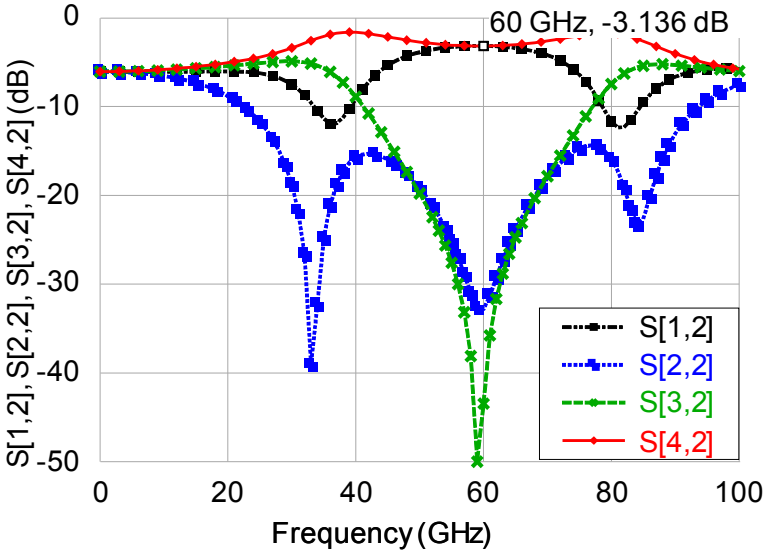

(b)

Fig 5. (a) Geometery and S-parameters of the designed coupler (b) S-parameter for port number2

sampling or using nonlinear devices. Nonlinear devices are categorized into two groups of (1) active devices such as Field Effect Transistor (FET) or Bipolar transistors and (2)

passive devices like Schottky diodes. Schottky diodes are preferred due to higher switching speed as compared to p-n junction diodes.

Fig. 6 represents the nonlinear behavior of this type of diodes. The non-linear behavior of Schottky diodes can be studied using Taylor series. Assuming output voltage $V_o(t) = a_0 + a_1 V_{in}(t) + a_2 V_{in}^2(t) + a_3 V_{in}^3(t) + \cdots$, where $V_{in}(t) = A\sin\omega_{LO}t + B\sin\omega_{RF}t$, the down-converted component at $(f_{RF} - f_{LO})$ frequency is generated by the second term, $V_{in}^2(t)$ which has a strong a2 component. This means that if they are excited properly, different mixing harmonics of the input signals are generated. For example, if F_{LO}=60GHz and F_{RF}=60.4GHz the F_{IF} of 0.4GHz can be extracted from the second term.

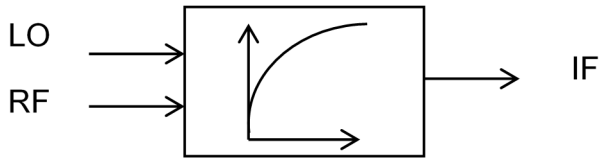

Fig 6. Nonlinear behavior of the diodes

A. FLIP-CHIP DUAL DIODE (GAAS DIODE)

Schottky diodes are majority carrier diodes and suitable for high frequency mixer due to their superior switching speed. They can be fabricated more precisely than PN-junction diodes. These are hot-carrier diodes, which possess low-noise and high conversion efficiency. Flip-chip dual diode is designed for high performance mixer applications. Main features of these diodes are high cut-off frequencies, high breakdown voltage, good ideality

factor, low cost and small size. The circuit equivalent of a Schottky diode junction is presented in Fig. 7.

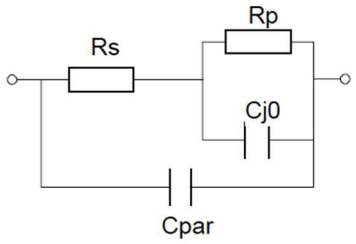

Fig 7. Circuit equivalent of the Schottky diode

where C_{par} and R_s are the packaging parasitic and R_p and C_{jo} are the non-linear components. Most diode mixer designs utilize unbiased diodes. Nevertheless, forward biasing of the diodes causes conversion losses especially when limited LO signal is available. The optimum operating point is the region that diode has maximum non-linearity in its characteristics.

The proposed method for 60GHz RFID utilizing a 180° ring hybrid coupler and a rat-race mixer is presented in Fig. 8. This technique supports direct conversion and allows a single mask fabrication process for both mixer and coupler. The mixer consists of two diodes arranged so that the local oscillator (LO) signal is 180° out of phase with the radio frequency (RF) signal in one of them but in the other diode with the signals are in-phase. The balanced operation results in LO noise suppression and provides large dynamic range and high intermodulation suppression. Microstrip mixers are preferred compared to other techniques such as waveguide, suspended stripline or finline, mainly due to inexpensive

fabrication process. In addition, they are more reliable and amenable for monolithic integration with other front-end circuitry for a compact RFID reader at 60GHz.

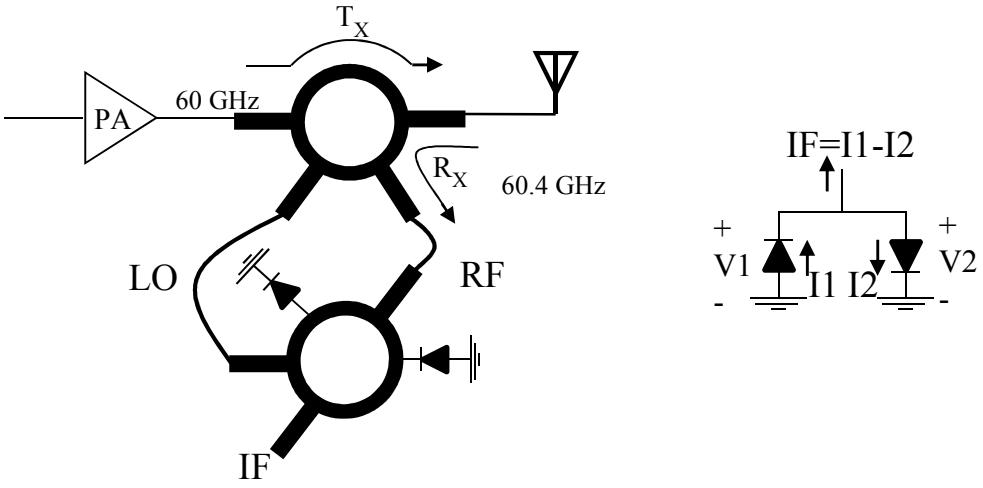

Fig 8. Configuration of 180° ring hybrid coupler combined with rat-race mixer

IF signal is calculated by subtracting $V_1 = V_{RF}\cos(\omega_{RF}t) + V_{LO}\cos(\omega_{LO}t + \pi)$ and $V_2 = V_{RF}\cos(\omega_{RF}t) + V_{LO}\cos(\omega_{LO}t)$ in $I_1 = aV_1 + bV_1^2 + cV_1^3 + \cdots$ and $I_2 = -aV_2 + bV_2^2 - cV_2^3 + \cdots$ in equation (14)

$$IF = I_1 - I_2 = [aV_1 + bV_1^2 + cV_1^3 + \cdots] - [-aV_2 + bV_2^2 - cV_2^3 + \cdots] =$$

$$a[V_{RF}\cos(\omega_{RF}t) + \cos(\omega_{LO}t + \pi)] + b[V_{RF}\cos(\omega_{RF}t) + V_{LO}\cos(\omega_{LO}t + \pi)]^2 + c[V_{RF}\cos(\omega_{RF}t) + V_{LO}\cos(\omega_{LO}t + \pi)]^3 + a[V_{RF}\cos(\omega_{RF}t) + V_{LO}\cos(\omega_{LO}t)] - b[V_{RF}\cos(\omega_{RF}t) + V_{LO}\cos(\omega_{LO}t)]^2 + c[V_{RF}\cos(\omega_{RF}t) + V_{LO}\cos(\omega_{LO}t)]^3 + \cdots \quad (14)$$

Extending the square terms of the Tylor series and looking for $(A cos\omega_{LO} t) \times (B cos_{RF} t)$ term, the up-converted and down converted components appear as $\frac{AB}{2}[cos2\pi(f_{RF} - f_{LO})t - cos2\pi(f_{RF} + f_{LO})t$ which contains the desires IF frequency of $f_{RF} - f_{LO}$ at 400MHz.

Drawbacks of this configuration are either (1) a close loop for one of the diodes which leads to a hole during fabrication process to ground the diode or (2) a non-secure and lossy wire bounding to ground the diode. This will raise the fabrication process price. Using two 180° Ring Hybrid Couplers causes at least 3dB if this structure is used for a reader.

Fig. 9 proposes a techniques to overcome these problems. In which only one ring is used to prevent the double division of the signals. The 60 GHz output signal can be sent to the object and also used to mix with the received signal with diodes to generate the desired IF signal.

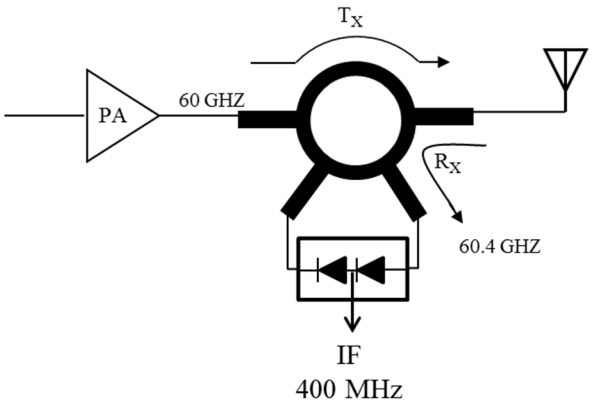

Fig. 9. Proposed combined coupler and mixer structure.

The following calculation presents the mathematical proof. Due to the symmetry, the ports have the same potential and therefore virtual ground as shown in Fig 10. The exponential nonlinearity of the diode junction can be expressed [9] by the power series

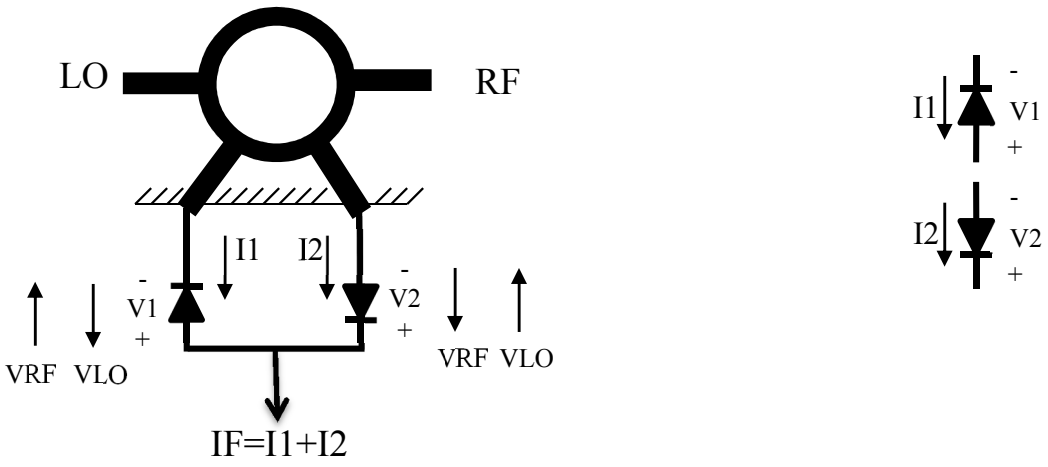

Fig. 10. Model of the proposed method.

Subtracting the $V_1 = V_{RF}\cos(\omega_{RF}t) - V_{LO}\cos(\omega_{LO}t)$ and $V_2 = AV_{RF}\cos(\omega_{RF}t) + BV_{LO}\cos(\omega_{LO}t)$ in $I_1 = aV_1 + bV_1^2 + cV_1^3 + \cdots$, and $I_2 = -aV_2 + bV_2^2 - cV_2^3 + \cdots$ IF signal can be calculated from sum of the I1 and I2, $IF = I_1 + I_2$.

The strong a_2 component of the IF signal is $bV_1^2(t) = b(V_{RF}cos\omega_{RF}t - V_{LO}cos\omega_{LO}t)^2$ which contains $-2b(V_{RF}cos\omega_{RF}t).(V_{LO}cos\omega_{RF}t)$ and after simplifications addition and subtraction of the RF and LO signal, $\frac{-2bV_{LO}V_{RF}}{2}[cos2\pi(f_{RF} - f_{LO})t - cos2\pi(f_{RF} + f_{LO})t]$. Finally, the desired IF frequency of $f_{RF} - f_{LO}$ at 400MHz is obtained.

A RF signal with a typical value of -100dBm at the center frequency of 60.4 GHz is applied to port 4 of the coupler. The output signal of the power amplifier which is a signal in the range of 10dBm at center frequency of 60 GHz is applied to the beam port number 2. Fig. 11 shows the mixed signal at the output port of the mixer.

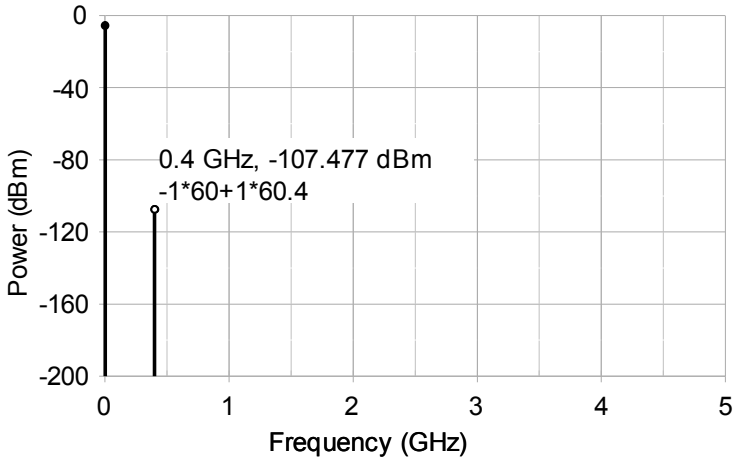

Fig. 11. Mixed signal at 0.4GHz

Conversion gain which is $CG=P_{IF}$ - P_{RF} is displayed in Fig. 12a. The RF power is swept from -120 to 20dBm for to obtain the loss of the coupler and mixer for different input power values. P_{1dB} compression presents the nonlinearity of the mixer which is shown in Fig. 12b, for the input RF signal power from -120dB to 20dB. This figure indicates that the mixer behaves linearly up to almost 0dBm.

Fig. 13a displays the relation between the output IF power signal and the LO signal. Sweeping the power of LO signal determines the boundary of the input LO power which is almost constant from 2dBm to 16dBm with a loss of less than 10dB. The best LO signal for lowest conversion gain happens at 15dBm with the gain of 7.2dB. The noise figure

computed from a harmonic balance noise simulation is a single sideband noise figure at 16.85C, which is the standard temperature for noise figure measurement as defined by the IEEE. IF port noise power at 400MHz for 1Hz frequency bandwidth is shown in Fig. 13b.

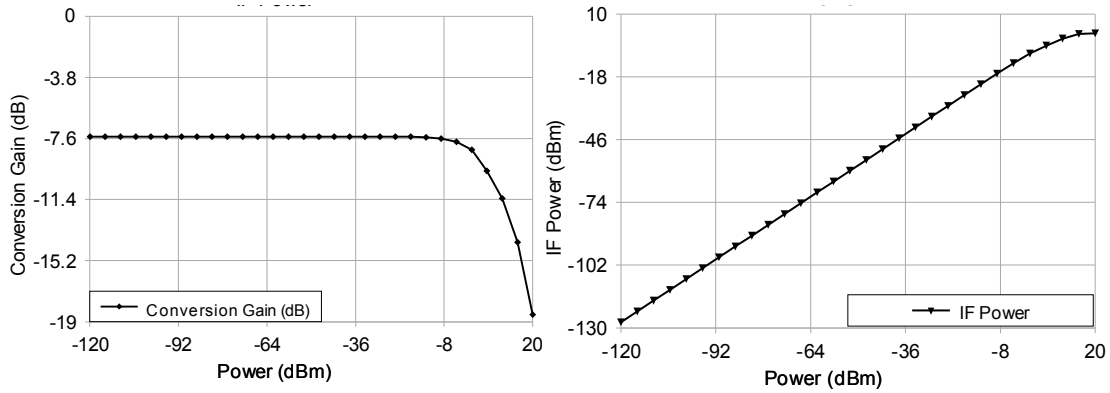

(a) (b)

Fig. 12. (a) Conversion Gain, (b) P_{1dB} compression.

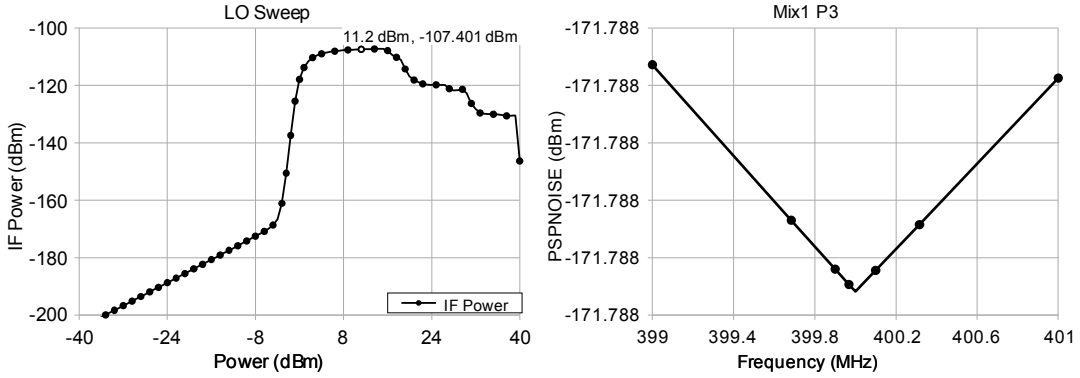

(a) (b)

Fig. 13. (a) IF signal over LO Sweep to determine the input boundary, (b) PSnoise at IF band.

III. CONCLUSION

The proposed structure allows the use one antenna array to send and receive signals which reduces the size and the costs of a reader. Using LTCC substrate at the millimeter-wave

frequency, a fully integrated 60 GHz transceiver can be implemented. The mixer and coupler module has one of the lowest conversion gain compared to passive mixers. The coupler presents -3.1dB insertion loss and better than -30dB return loss at center of 60GHz. Passive microwave mixer utilizing flip-chip dual GaAs diode exhibits a conversion gain of -7.47 dB.

REFERENCES

[1] Pursula, P.; Karttaavi, T.; Kantanen, M.; Lamminen, A.; Holmberg, J.; Lahdes, M.; Marttila, I.; Lahti, M.; Luukanen, A.; Vähä-Heikkilä, T., "60-GHz Millimeter-Wave Identification Reader on 90-nm CMOS and LTCC," Microwave Theory and Techniques, IEEE Transactions on , vol.59, no.4, pp.1166,1173, April 2011

[2] Pursula, P.; Vaha-Heikkila, T.; Muller, A.; Neculoiu, D.; Konstantinidis, George; Oja, A.; Tuovinen, J., "Millimeter-Wave Identification—A New Short-Range Radio System for Low-Power High Data-Rate Applications," Microwave Theory and Techniques, IEEE Transactions on , vol.56, no.10, pp.2221,2228, Oct. 2008

[3] C. Wagner, H. P. Forstner, G. Haider, A. Stelzer, and H. Jager, “A 79-GHz Radar Transceiver with Switchable TX and LO Feedthrough in a Silicon-Germanium Technology,” *IEEE BCTM 7.1*, pp. 105–108, 2008.

[4] M. Hartmann, C. Wagner, K. Seemann, J. Platz, H. Jager and R. Weigel, “A Low-Power Micromixer with High Linearity for Automotive Radar at 77 GHz in Silicon-Germanium Bipolar Technology,” *IEEE conference*, pp. 237–240, 2007.

[5] T. P. Budka, D. Antopolsky and M. T. Pizzella, “A 76 to 77 GHz GMIC Mixer for Automotive Radar,” *Microwave Journal Frequency Matters*, pp. 1–3, 2000.

[6] Avago Technologies, “Low Cost Mixer for the 10.7 to 12.8 GHz Direct Broadcast Satellite Market,” *Application note 1136,* Jan 2010.

[7] Feger, R.; Wagner, C.; Schuster, S.; Scheiblhofer, S.; Jager, H.; Stelzer, A., "A 77-GHz FMCW MIMO Radar Based on an SiGe Single-Chip Transceiver," Microwave Theory and Techniques, IEEE Transactions on , vol.57, no.5, pp.1020,1035, May 2009.

[8] Schoebel, J.; Buck, T.; Reimann, M.; Ulm, M.; Schneider, M.; Jourdain, A.; Carchon, G.J.; Tilmans, H.A.C., "Design considerations and technology assessment of phased-array antenna systems with RF MEMS for automotive radar applications," Microwave Theory and Techniques, IEEE Transactions on , vol.53, no.6, pp.1968,1975, June 2005.

[9] S. A. Mass, Microwave Mixers, 2nd Edition, *Artech House*, 1993.

[10] M. I. Skolnik, Introduction to Radar Systems. New York: McGraw Hill, 2001.

[11] D. M Pozar, Microwave Engineering 3nd edition, New York: J. Wiley and Sons, 2005.

Chapter 6

Programmable Chipless Radio Frequency Identification Tag Using RF MEMS Switches

RFID technology is rapidly expanding [1-6] and RFID systems are vastly employed in many applications including supply management, smart identification, passport/portal authentication, logistics, tracking, location positioning, and security. In an RFID system radiated signal from reader is used to supply the transponder. A transponder or tag needs to be within the communication range in order to generate the required dc voltage for operation from the induced reader signal to its antenna [1].

Typically, the induced voltage across a UHF tag antenna is about 0.1V to 0.3V. This voltage is not enough to power up the tag circuitry and needs to be increased. The voltage provided by the antenna depends on the source resistance and reactance. The source resistance depends on the antenna configuration and can vary from a few tens to a few hundred ohms. A typical load can be modeled by a resistor varying from 1.0 kΩ to 0 kΩ.

To match the source and load impedances an LC circuit can be used. Such a matching circuit can theoretically provide a voltage gain proportional to the square root of the ratio of the source and load impedances. This method can increase the voltage by a factor equal to the quality factor, Q, of the matching circuit. For instance for Q=10 the voltage across the load is increased by ten. Using reactive matching, an increase of 5- to 10-fold in the antenna voltage can be achieved. Communication between a UHF tag and a reader takes place based on the principle of backscattering [3].

Although RFID technology has been successful and in spite of significant progress in the area of radio frequency identification, RFID tags have not been able to replace barcode labels. This is mainly due the costs involved in manufacturing RFID tags. In general, RFID tags require microelectronic chips which make them less cost-effective compared to barcode labels. Many solutions have been proposed in literature to implement chipless RFID tags to reduce the costs and enable RFID tags to compete with barcode labels. An array of antennas or multi-resonators has been utilized as a low-cost chipless tag [1, 7]. However, this solution requires operation at gigahertz range to reduce the size of antenna elements.

In [8], RFID tags using multiple frequency bands of 2.4GHz, 5.25GHz and 5.8GHz, are presented. These tags contain arrays of microstrip antennas resonating at different frequencies.

In [9], low-cost chipless tags using printable tag with electromagnetic codes using split ring resonators is proposed where electromagnetic characteristics of split ring resonators

are used for identification. However, most of the available chipless tags are not programmable and different masks are required for their implementation.

In this work MEMS technology is utilized to design a low-cost programmable RFID tag which can operate on the standard UHF band for RFID applications. A basic low-cost MEMS fabrication process with two metal layers has been used to implement a chipless RFID tag. Programmable MEMS switches are utilized to backscatter a unique pattern from each tag to identify an object, Fig 1. The rest of the paper is organized as follows. Section II presents details of the proposed method and the principle of operation for one-bit MEMS switching module as well as N-bit chipless programmable tags. Implementation of a MEMS switching module for a 3-bit chipless tag is presented in section III followed by fabrication process in section IV. Simulation and measurement results are presented in section V and finally the conclusions are summarized in section VI.

III. PROPOSED STRUCTURE

Communication between RFID UHF tags and interrogators is commonly performed through signal backscattering. In this method, the transmitted signal is backscattered to the RFID reader when the tag antenna is connected to a small load. Whereas the tag antenna is open or connected to a large load, the tag does not radiate back the signal. In fact the tag's control circuit simply turns on and off a switch between the tag's antenna and ground to communicate with the readers. In a conventional UHF RFID tag, a chip is used to control the tag's switching activities and pattern the backscattered signal [10, 11].

In the proposed method in this paper, the backscattered signal is patterned by an array of MEMS-switching module. Each switching module can connect the tag antenna to the ground path for a short period of time to backscatter the incoming signal.

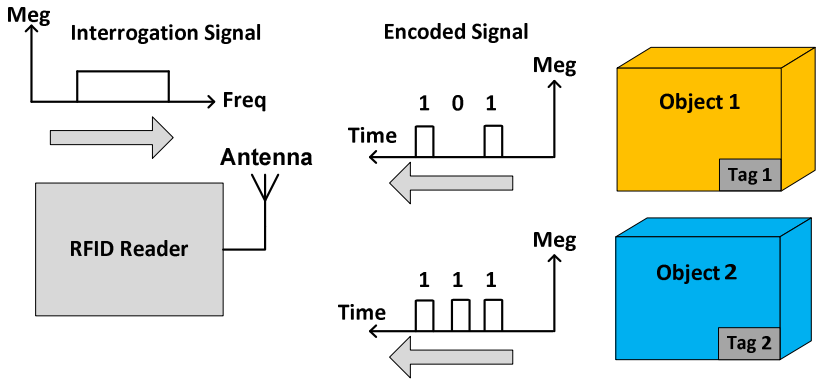

Fig. 1. Chipless RFID architecture.

Fig. 2 shows a switching module which includes two MEMS switches with different pull-in voltages of V_1 and V_2. When the control voltage, V_{cntl} exceeds V_1 the first switch, SW_1, turns on and connects the antenna to ground. The antenna path to ground remains closed until the input voltage exceeds V_2 when the second switch, SW_2, turns on and connects node A to ground. As a result SW_1 is turned off and the antenna path to ground is opened. The antenna backscatters the interrogator's signal for a period of time when $V_1 < V_{cntl} < V_2$ and the antenna path to ground is closed.

The MEMS module in Fig. 2 can be used to communicate one-bit information. A number of MEMS- switching modules with different pull-in voltages can be utilized to backscatter several bits of information to the reader.

To communicate with the tag using the proposed MEMS switching module two conditions have to be met. First, the transmitted signal by reader has to be amplitude modulated and second the voltage across the switching module has to exceed the pull-in voltages of the implemented MEMS switches to ensure proper switching. The first condition can readily be satisfied by modulating the transmitted signal using a single tone. To satisfy the second condition the tag's antenna and the MEMS switches have to be carefully designed. The control signal at the input of the switching module in Fig. 3 has to be generated by tag's antenna. This signal should be high enough to turn-on MEMS switches. However, the antenna of a conventional UHF RFID tag provides an open-circuit voltage of about 0.1-0.3V, which is not high enough to turn on a typical MEMS switch.

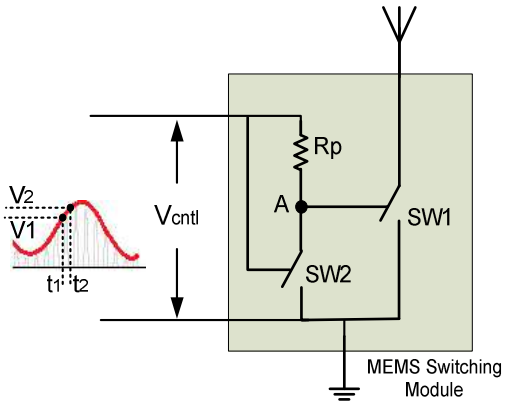

Fig. 2. One-bit MEMS switching module.

To overcome this problem, a resonant circuit is utilized to increase the antenna voltage. The tag antenna's Thevenin equivalent circuit with induced electromagnetic wave, V_{ant}, across the antenna is modeled in Fig. 3. Lumped model of the antenna contains a

resistor, R_{ant}, an inductor, L_{ant} and a ohmic resistor of R_s. Therefore the antenna impedance is $Z_{ant} = R_s + R_{ant} + j\omega L_{ant}$. If the antenna is connected to a capacitive load, C_{load}, with a shunt resistance , R_{load}, it can be shown that the voltage across the load increases by the quality factor (Q) of the LC tank at the resonant frequency.

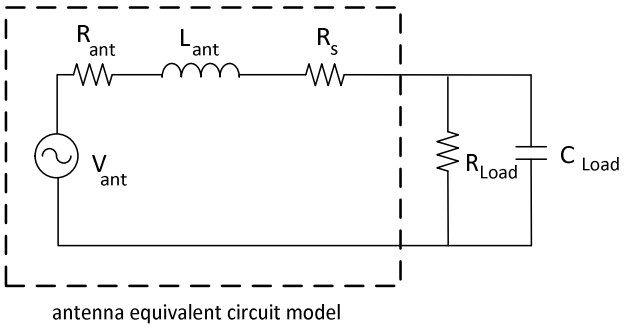

Fig. 3. Resonant circuit to increase antenna voltage at the load

The current flowing through the circuit, I_{ant}, at the resonant frequency is given by $I_{ant} = V_{ant}/(R_s + R_{load} + R_{ant})$ and the voltage across the load, V_{load}, is determined from equation (1),

$$V_{load} = I_{ant} \times Z_{load} = \frac{V_{ant}}{R_{eq}} \times \frac{1}{C_{load}\omega} = V_{ant} \times Q \tag{1}$$

where $R_{eq} = R_s + R_{load} + R_{ant}$ and Q is the quality factor given by

$$Q = \frac{1}{R_{eq} C_{load} \omega} = \frac{L_{ant}\omega}{R_{eq}} \tag{2}$$

From (1) it can be seen that the voltage across the load is Q times of the antenna voltage. This technique can be used to increase the antenna voltage to provide enough electric potential to activate a MEMS switch with a low pull-in voltage.

Fig. 4 shows a simplified diagram of the proposed chipless RFID. It includes a receiving antenna which is represented by its equivalent circuit together with an envelope detector, two MEMS switches and a transmitting antenna. Such a basic structure can be used to communicate one-bit information by turning on and off SW_1 using the induced voltage across the receiving antenna. The antenna reactance, X_{ant}, is matched with a capacitor, C_1 in Fig. 4 to increase the level of voltage across the MEMS switches. Considering the input impedance of the tag as Z_{in}, the tag reflection coefficient can be determined from $\Gamma_{tag} = \frac{Z_{ant} - Z_{in}^*}{Z_{ant} + Z_{in}}$. In order to minimize the signal reflection, the antenna and the load have to be matched and satisfy $Z_{ant} = Z_{in}^*$.

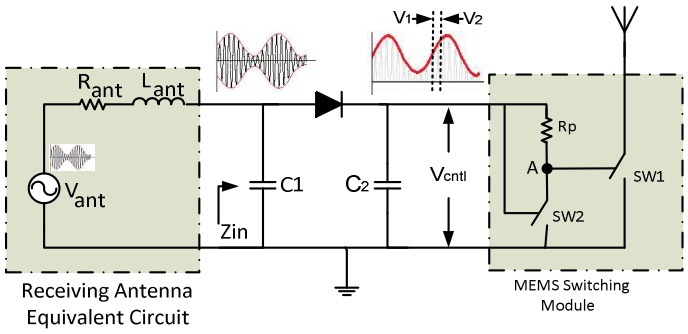

Fig. 4. Chipless tag using two MEMS switches to send one-bit information through backscattering. The received signal is backscattered when $V_1 < V_{cntl} < V_2$.

A. N-bit Chipless Programmable Tag

A N-bits chipless tag using 2N MEMS switches is presented in Fig. 5. The MEMS switches in each module are designed to turn-on for a particular time slot defined by their pull-in voltages. As a result, each switching module connects the antenna to the ground in a certain time slot when the signal across C_2 falls within the pull-in voltages of its pair of MEMS

switches. The MEMS switches are designed to distribute N-bits of information over one period of the envelope signal transmitted by reader. The tag can be programmed to a unique backscattering pattern or code by burning the MEMS fuses [12] connected to the switching modules and break the paths to ground. In the designed chipless tag, fuses were implemented using a high resistivity layer to allow a basic tag programming. To burn a fuse, a high voltage can be applied to the microstrip line connected to the high resistivity layer to increase the temperature beyond its melting point.

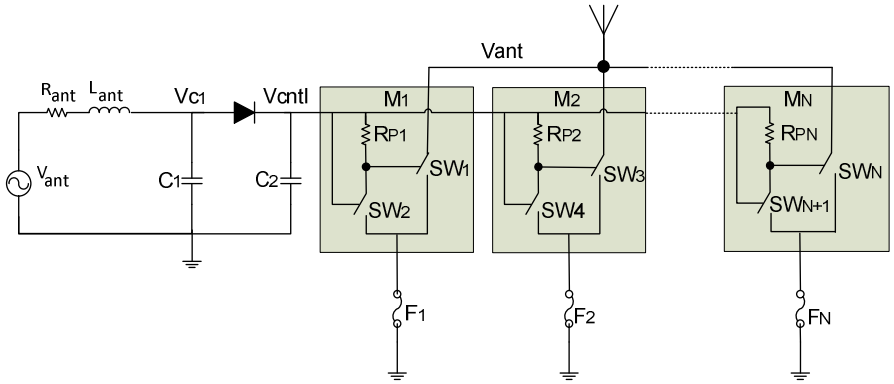

Fig. 5. Schematic diagram of a N-bit chipless tag.

B. Reading Range

For a matched impedance tag, power available for a tag at distance r using the Friis equation becomes [11]:

$$P_{RX} = P_{TX} G_{RX} G_{TX} \cos^2(\theta_{plo}) \left(\frac{\lambda}{4\pi r}\right)^2 \tag{3}$$

Where P_{RX} is the received power, P_{TX} is the transmitted power, G_{RX} and G_{TX} are antenna gain of transmitter and receiver, λ is wavelength and $cos^2(\theta_{plo})$ is the polarization mismatch factor. To calculate the communication-link power-budget, a 90° polarization

between transmitting and receiving antenna is considered to increase the polarization effect on induced voltage. P_{RX} should be high enough to fulfill the operation requirements. The tag has to send an encoded signal with enough power to exceed the minimum detectable power of the reader. Using Friis equation, the received power at the reader [11] can be driven from

$$P_{RX,reader} = P_{TX,reader} T_b G_{reader}{}^2 G_{tag}{}^2 (\frac{\lambda}{4\pi r})^4 \tag{4}$$

where T_b is the transmission loss, G_{tag} is the gain of tag antenna and G_{reader} is the gain of reader antenna. The maximum reading range, r_{max}, of the reader can be determined from

$$r_{\max} = (\frac{\lambda}{4\pi})^4 \sqrt{\frac{P_{TX,reader} T_b G_{reader}{}^2 G_{tag}{}^2}{P_{\min,reader}}} \tag{5}$$

where $P_{min,reader}$ is the minimum required signal power for demodulation at the reader. The proposed chipless RFID tag contains MEMS modules, rectifier and loop antenna. The power received and transmitted by the tag is a function of the frequency and thus the maximum reading range depends on the readers frequency as shown in Fig. 6.

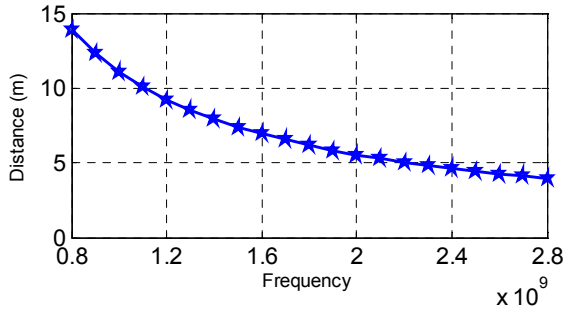

Fig. 6. Reading distances over different frequency range.

C. Collision Detection

The collision can be avoided using digital or analog beamformer techniques to scan the location and send narrower signals to distinctly detect the backscattered signal from a tag at the time domain. This method is called space division multiple access (SDMA). The second method is based on the FMCW radar technique utilizing the time difference of arrival (TDOA) of response signals from different tags. The first solution requires hardware component for implementation and the second one can be implemented with software using digital signal processing techniques.

IV. TAG IMPLEMENTATION

MEMS switches have many advantages over semiconductor or mechanical switches for implementation of RFID tags. They present high isolation, low DC power consumption and their sizes and fabrication costs are relatively low. MEMS microscale switches can be fabricated in mass quantities using a basic and inexpensive MEMS processes. They consume almost zero power as they operate based on electrostatic forces between positive and negative charges and they don't draw current from the source [13]. The components in Fig. 5, can be implemented using a basic fabrication process containing two metal layers and one resistive layer. To implement the tag, MEMS switches with different pull-in voltages are needed. There are different structures to implement a MEMS switch; among them cantilever switch supports a relatively low pull-in voltage [14-16]. The pull-in voltage, $V_{pull-in}$, of a MEMS switch can be calculated from equation (6),

$$V_{pull-in} = \sqrt{\frac{8K_Z g_0^3}{27W\varepsilon_0}} \quad (6)$$

where K_z is the spring constant, g_0 is the gap between metal plates, W is the area of the pads and ε_0 is the air permittivity.

For the purpose of RFID tag implementation, it is highly desired to reduce the pull-in voltage of MEMS switches. The voltage applied to the MEMS switches are generated from the induced voltage across tag antenna. A high pull-in voltage requires a high quality antenna to increase the voltage through reactive matching [6]. The pull-in voltage, equation (6), can be reduced by three different methods of (a) increasing the area of the pads, W. (b) reducing the gap between metal plates, g_0, and (c) reducing the spring constant K_z. There is trade-off between the size of the MEMS switch and its pull-in voltage. To lower the pull-in voltage, the size of the MEMS can be increased.

A MEMS switch can be implemented using either fixed to fixed beam structure [14] or cantilever beam actuator. Fixed to fixed MEMS switches as compared to cantilever switches support larger electrode areas and therefore larger actuation capacitances. Whereas cantilever structures support lower pull-in voltages [13]. Cantilever MEMS switches have been utilized in this work to implement a chipless RFID tag. Fig. 5 shows an implemented MEMS switch with pull-in voltage of 1.5V in which a resistive layer is used to implement the fuse. The gap between the plates of all switches are chosen to be 1.5um to support high isolation as well as low insertion loss. The same structure with

different cantilever lengths is used to implement switches with different pull-in voltages. The spring constant K_z in the z-direction can be determined from equation (7) [16].

$$K_z = EW\left(\frac{t}{L_c}\right)^3\left\langle 1+\frac{L_s}{L_c}\left\{\left(\frac{L_s}{L_c}\right)^2+12(1+\upsilon)\left[1+\left(\frac{W}{t}\right)^2\right]^{-1}\right\}\right\rangle^{-1} \quad (7)$$

where E and ν are the Young's modulus and Poisson's ratio of the metal, respectively. Lc and Ls are the length of the cantilever and the spring respectively. W and t are width and thickness of the cantilever [16]. Current distribution is mostly concentrated on the edge of the cantilever beam, therefore placing some small holes in the beam improves the switching time [14-16].

A 1.5um gap between dimple and transmission line provides enough isolation in the OFF state. In this state a high isolation can be achieved by increasing the initial gap or reducing the size of the contact area. Fig. 7 presents the electrical model of a single switch in OFF and ON states. In OFF state there is a series capacitor, C_s , between the output transmission line and cantilever dimple. There are two parasitic capacitances of C_{p1} and C_{p2} between the output, input and actuation pad. The RL equivalent of the switch in ON state is shown in Fig 7b. R_{cs} and R_l are the contact resistance and cantilever resistance of the switch. The metal conductivity, size of the contact area and the applied force determine the contact resistance. The total switch resistance is $R_s = R_l + R_c$. The total power loss of the switch is $P_{loss} = R_s I_s^2$ [3]. The intrinsic loss of the cantilever can be driven from $Loss = \frac{4R_s Z_0}{|Z_s+2Z_0|^2}$ [16]. In the ON state, impedance is $Z_s = R_s + j\omega L$, and for RF frequencies $\omega L \ll Z_0$ and

therefore $Loss = \frac{R_s}{Z_0}$. In the OFF sate, isolation can be calculated from $S_{21} = \frac{2j\omega C_u Z_0}{1+2j\omega C_u Z_0}$, where $C_u = C_s + (C_{p1} \times C_{p1}/((C_{p1} + C_{p1}))$.

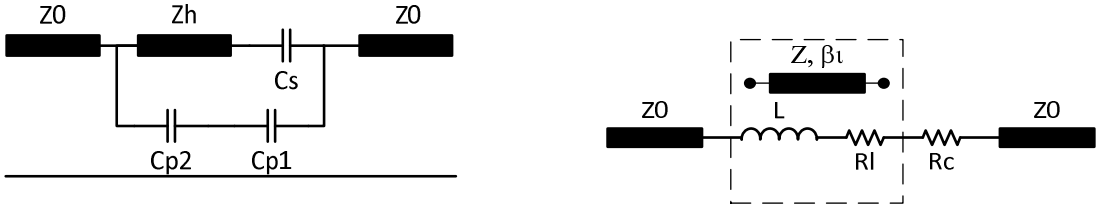

(a) (b)

Figure 7. Present the electrical model of a single switch in (a) OFF and (b) ON states

V. FABRICATION PROCESS

The MEMS module was implemented using a research-oriented, cost effective fabrication process. This process can be used for batch fabrication of the programmable chipless RFID tags. The microfabrication process includes eight steps as shown in Fig. 8. It is started with a 635um thick Alumina substrate with loss tangent of 0.0001 at 1MHz and relative permittivity of 9.9. Electron beam write chromium masks are used during fabrication process. In the first stage after polishing and RCA substrate cleaning, 50nm Titanium tungsten (TiW) bias line is sputtered and patterned. TiW is used for highly resistive traces (HRT) to connect the DC bias pads to the fixed and movable actuation pads. This stage is followed by deposition of 0.7um SiO_2 at 250^{o}C by plasma enhanced chemical vapor deposition (PECVD) which is patterned using reactive ion etching (RIE). Then a seed layer is deposited by evaporating 40nm Cr/70nm Au bilayer. A negative photoresist (PR) mold is patterned using 1μm Au which is electroplated inside that mold by photolithography.

The Cr layers are washed out because they are only an adhesion layer for Au. The fabrication process is followed by 0.7µm SiO2 PECVD deposition at 250˚C as dielectric. A 30nm of TiW is then used as an adhesion layer between D2 and G1.

In step five a 2.5µm thick spin coated polyimide layer is used as a sacrificial layer. In order to have anchor and dimple holes, polyimide is patterned using RIE. Then 70nm Au is sputtered as a seed layer and electroplated Au layer with total thickness of 2um is added. Finally, the sacrificial layer is removed using O2 plasma dry etching in RIE.

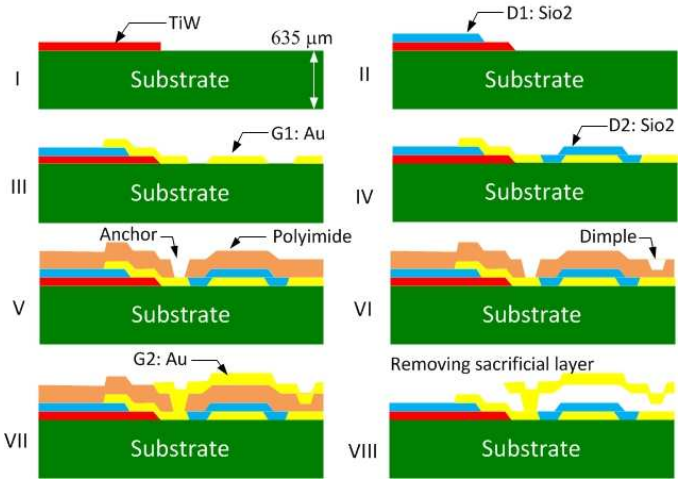

Fig. 8. Fabrication Process

VI. Simulation and Measurement Results

Implemented RF MEMS switch using two layers of metal and a dielectric layer is presented in Fig. 9(a). Fig 9(b) displays a RF MEMS switch is excited with 1.5V. Simulation results using Coventorware^{TM} indicate a displacement of 1.5um at the tip of the switch.

The MEMS switch in ON and OFF states is simulated using finite difference time domain (FDTD) simulator of EMPro software. As expected, the results of FDTD simulator show

that the switch has a small S_{21} and a high S_{11} in the OFF state while in the ON state contrary to the OFF state, S_{21} is high and S_{11} is low as shown in Fig.10. Simulation results indicate that the insertion loss and the isolation of the implemented switches are about -0.01dB and -60dB, respectively, at 910MHz frequency when the switch is OFF. In the ON state the insertion and return losses are -0.1dB and -49dB at center frequency.

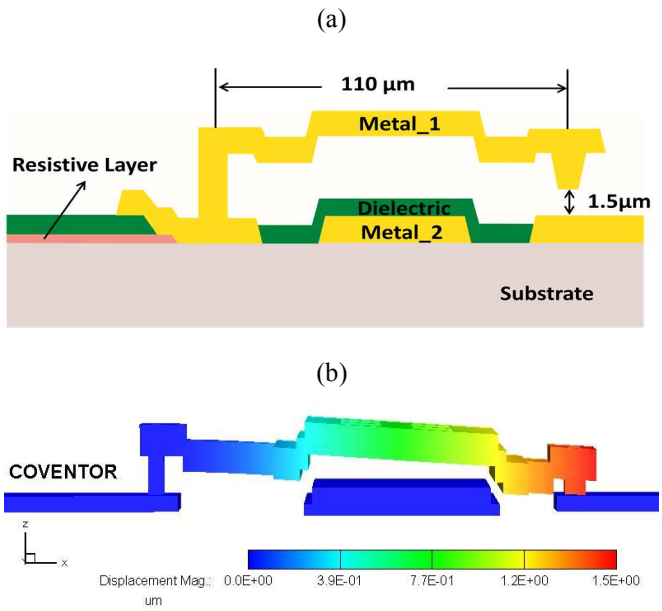

Fig. 9. (a) Implemented MEMS switch with 1.5V pull-in voltage, (b) displacement at pull-in voltages for first contact of the switch in 3D geometry using Coventorware™.

Fig 11. presents the measurement setup for the MEMS switch which includes E5061B Network Analyzer from Agilent and MA-8100 RF probes from SEMIPORBETM.

Fig. 12 presents the S-parameter measurement results of a MEMS RF switch under test using MA-8100 RF probes in ON and OFF states.

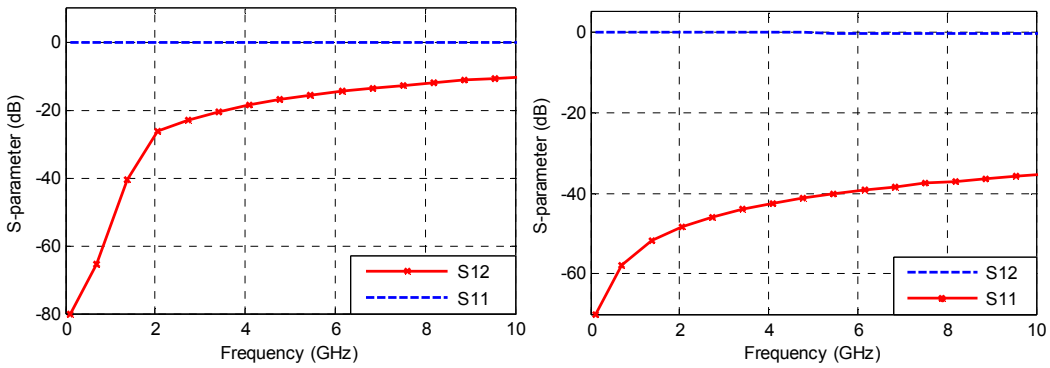

(a) (b)

Figure 10. S-parameters of MEMS switch in (a) OFF and (b) ON states

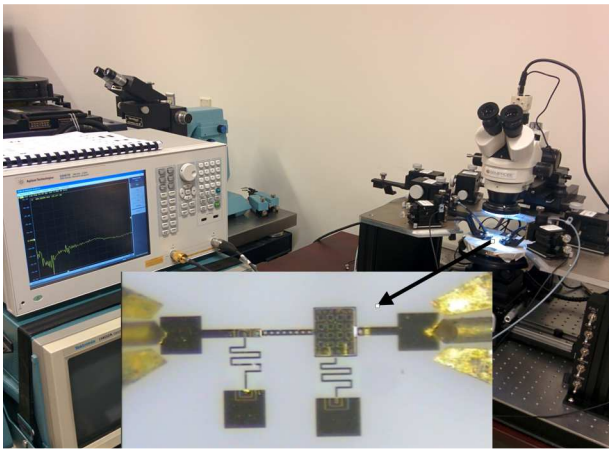

Fig 11. A RF MEMS switch under measurement setup using E5061B 100k-3GHz ENA Series Network Analyzer using MA-8100 RF probes from SEMIPORBE™.

Design parameter variations such as material properties or dimension changes, which might vary during different production runs, can be evaluated using Coventorware for reliability analysis. Parametric analysis is conducted to study the effect of the Young's Modulus on the pull-in voltage of the RF MEMS switch. Fig. 13 shows the variation of Young's Modulus by 5% from 90% to 100% in three steps for G2 layer. This study shows the stiffness of the beam by means of reducing the Elastic Constant of the Gold material.

The reduction in the Young's Modulus (E elastic constant) reduces the required voltage to achieve enough pull-in or displacement. The displacement of the switch with respect to 100% Young's Modulus at 1.4V increases by 12.79% and 31.03%, for Young's Modulus of 95% and 90% respectively.

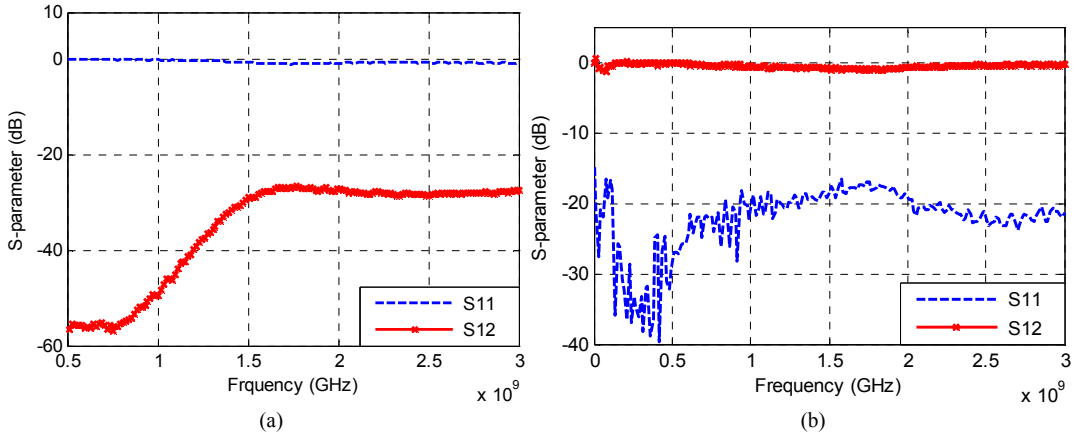

Fig. 12. S-parameter measurement results of a MEMS RF switch under test using MA-8100 RF probes in (a) OFF and (b) ON states.

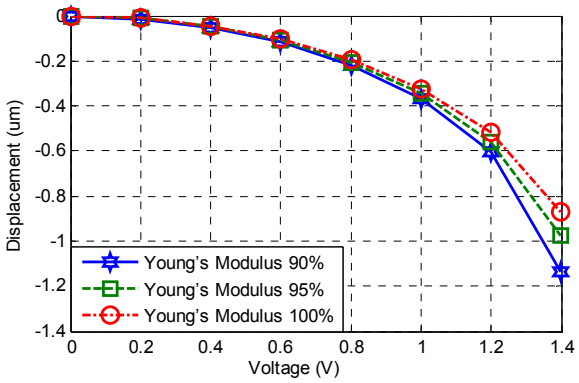

Fig. 13. Displacement variation based on Young's Modulus reduction.

Fig. 14 shows the displacement vs voltage for variation of the fabrication process up to 10%. Parametric analysis indicate that 0.1V to 0.2V variation in the pull-in voltage occurs

due to the process variations. However, this will shift the pull-in voltages of the switches in proposed chipless tag and will and therefore will not impact the tag performance.

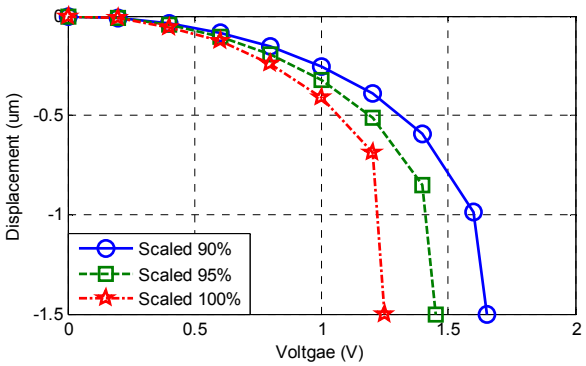

Fig. 14. Dimension changes analysis due to the fabrication process variation by up to 10% in very inexpensive method of fabrication process for whole switch size.

A 3-bit chipless tag based on the diagram presented in Fig. 5 was implemented to test the tag response to a signal transmitted by an RFID reader. The layout and 3D view of the implemented switching modules designed using finite element analysis (FEA) tools with Coventorware software package is shown in Fig. 15.

Table 1 shows the dimensions of the MEMS switches used to encode 3-bit information. The pull-in voltages versus the displacements of the implemented MEMS switches in Fig. 16 show that the difference between the pull-in voltages of successive MEMS switches is about 0.2 volt.

Fabricated switching modules for a 3-bit chipless tag, using a commercial available tag antenna is shown in Fig. 17. The measured S-parameters of the antenna in ON and OFF states in are shown in Fig. 18.

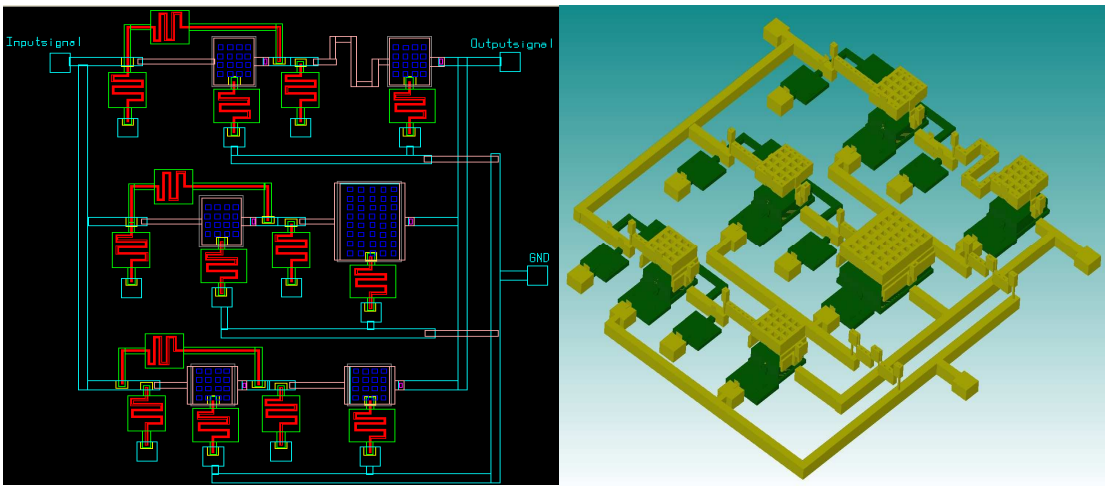

(a) (b)

Fig. 15. (a) Layout of the six MEMS switch with different pull-in voltage (b) 3D view of the implemented MEMS switching modules for a 3-bit chipless tag.

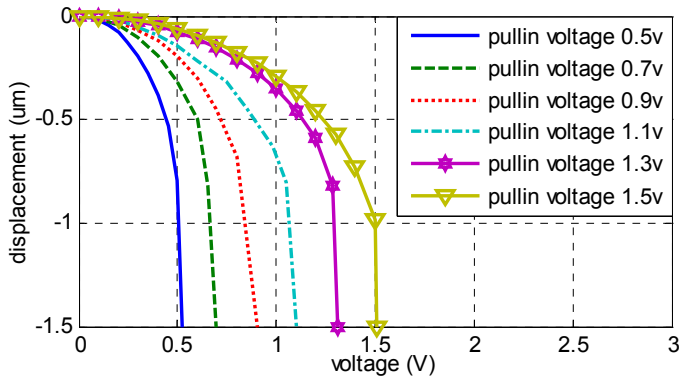

Fig. 16 Pull-in of the MEMS switches.

Table1. Dimensions of the implemented switches

	Restoring Spring Length×Width (µm)	Actuation Pad Length×Width (µm)
SW_1	700×30	190×220
SW_2	140×30	285×400
SW_3	235×30	190×220
SW_4	235×30	190×200
SW_5	135×30	190×200
SW_6	110×30	240×200

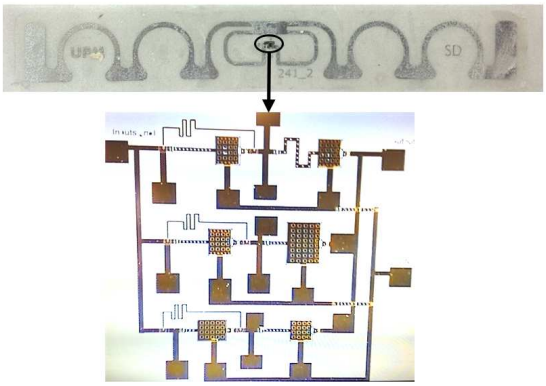

Fig. 17. Commercial available antenna and fabricated MEMS switching modules for a 3-bit chipless tag.

(a)

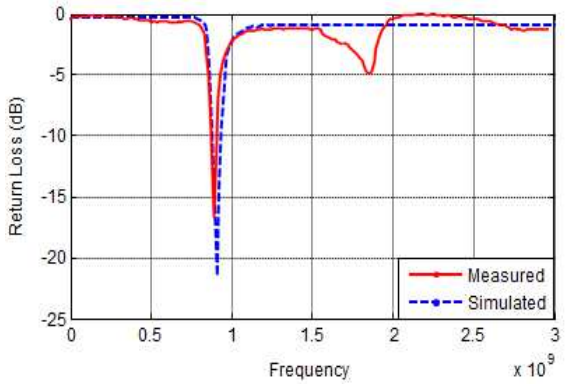

(b)

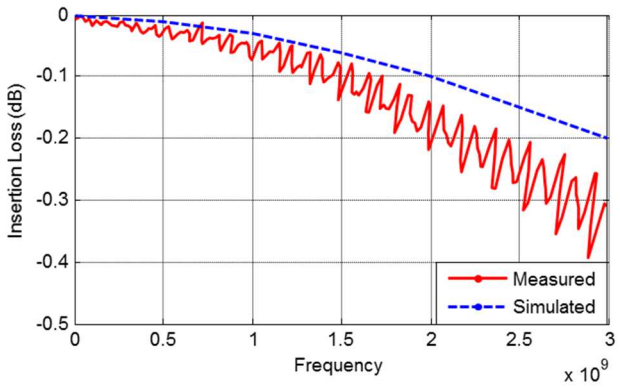

Fig. 18 Simulated and measured (a) return and (b) insertion loss.

To validate the operation of the implemented tag, the spice models of the switches were extracted and used to implement the circuit in Fig. 5 using ADS software package. A

910MHz carrier signal modulated with a 1KHz sinusoidal waveform with an amplitude of 0.2V was applied to the circuit. Two different tags with identification (ID) codes of 111 and 101 were used to perform the simulation. Fig. 19 illustrates the applied signal, V_{oc}, the output signal of the reactive matching circuit, V_{c1}, the output of the envelope detector, V_{cntl}, and the voltage across the output antenna, V_{ant}.

(a)

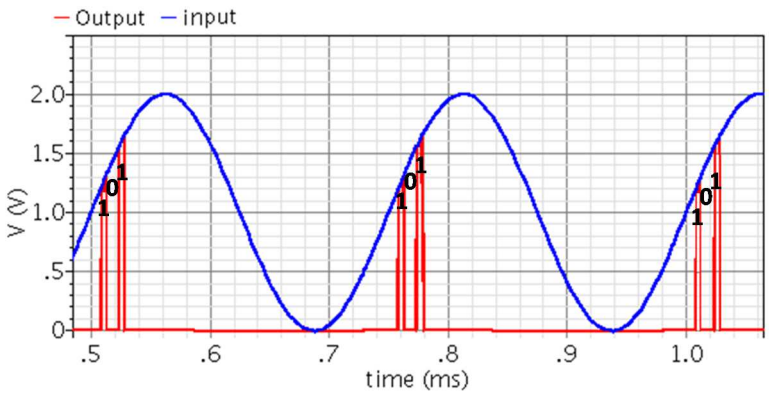

(b)

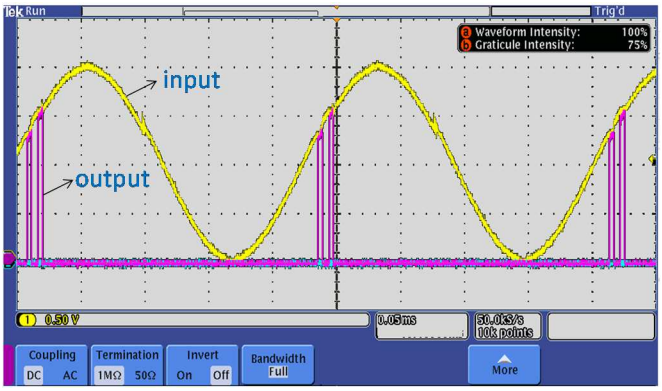

Fig. 19. Transient response of the chipless tag using 3-bit MEMS switching modules. (a) Simulation results for a tag with 101 identification code. (b) Measurement results

It can be seen that the matching circuit increases the level of the input signal by a factor of about 12. The envelop detector recovers the transmitted signal and provides the

switching modules with a low frequency signal which exceeds the threshold of MEMS switches. The outputs of V_{out1} and V_{out2} show that the tags detect the incoming signal and backscatter their identification codes.

VII. CONCLUSION

This paper presents a new method to implement low cost chipless RFID tags using MEMS technology. To the best of authors' knowledge, this is the first reported chipless RFID tag using MEMS technology. The proposed tags can be batch-fabricated using a basic MEMS fabrication process. The elimination of the chip, which accounts for the major portion of the RFID tag costs, can reduce the tag price to become an alternative to barcode labels. Simulation results using a 3-bit chipless tag indicate that the tag can backscatter the signal transmitted by an RFID interrogator. The employed MEMS switches can also be programmed to ensure that each tag has a unique backscattering pattern or identification code. 3-bit MEMS chipless tag is fabricated and tested using E5061B 100k-3GHz ENA Series Network Analyzer and probe station form SEMIPORBE™.

ACKNOWLEDGMENT

The authors would like to thank the research and financial supports received from Natural Sciences and Engineering Research Council (NSERC) of Canada and CMC Microsystems.

REFERENCES

[1] S. Preradovic, S. M. Roy, N. C. Karmakar, "RFID System Based on Fully Printable Chipless Tag for Paper-/Plastic-ltem Tagging", Antennas and Propagation Magazine, IEEE , Oct. 2011, 53, (5), pp. 15-32.

[2] S. Preradovic, I. Balbin, N. C. Karmakar, G. F. Swiegers, "Multiresonator-Based Chipless RFID System for Low-Cost Item Tracking", Microwave Theory and Techniques, IEEE Transactions on , May 2009, 57, (5), pp.1411-1419.

[3] K. Finkenzeller, RFID Handbook: Fundamentals and Applications in Contactless Smart Cards and Identification, 2nd ed. New York:Wiley, 1999, pp. 117–126, 143–148, 183–186.

[4] Y. F. Weng, S. W. Cheung, T. I. Yuk, L. Liu, "Design of Chipless UWB RFID System Using A CPW Multi-Resonator", Antennas and Propagation Magazine, IEEE , Feb. 2013, 55, (1), pp. 13-31.

[5] M. S. Bhuiyan, A. Azad, N. Karmakar, "Dual-band modified complementary split ring resonator (MCSRR) based multi-resonator circuit for chipless RFID tag", Intelligent Sensors, Sensor Networks and Information Processing, 2013 IEEE Eighth International Conference on , April 2013, pp. 277-281, 2-5.

[6] I. J. G. Zuazola, A. Sharma, J. C. Batchelor, A I. ngulo, A. Perallos, W. G. Whittow, J. M. H. Elmirghani, R. Langley, "Radio frequency IDentification miniature interrogator antenna sprayed over an in-vehicle chassis", Microwaves, Antennas & Propagation, IET, December 2012, 6, (15), pp. 1674-1680.

[7] P. Kalansuriya, N. C. Karmakar, E. Viterbo, "On the Detection of Frequency-Spectra-Based Chipless RFID Using UWB Impulsed Interrogation", Microwave Theory and Techniques, IEEE Transactions on, Dec. 2012, 60, (12), pp. 4187-4197.

[8] I. Jalaly, I. D. Robertson, "RF barcodes using multiple frequency bands", Microwave Symposium Digest, 2005 IEEE MTT-S International, June 2005, pp. 12-17.

[9] J. Hyeong-Seok, L. Won-Gyu, O. Kyoung-Sub, M. Seong-Mo, Y. Jong-Won, "Design of Low-Cost Chipless System Using Printable Chipless Tag With Electromagnetic Code", Microwave and Wireless Components Letters, IEEE, Nov. 2010, 20, (11), pp. 640-642.

[10] A. Vena, E. Perret, S. Tedjini, G. E. P. Tourtollet, A. Delattre, F. Garet, Y. Boutant, "Design of Chipless RFID Tags Printed on Paper by Flexography", IEEE Trans. on Ant. and Propag., 2013, 61, (12), pp. 5868–5877.

[11] D. M. Dobkin, 'The RF in RFID: Passive UHF in Practice' (Elsevier, 2008).

[12] Y. S. Chiu, K. S. Chang, R. W. Johnstone, M. Parameswaran, "Fuse-tethers in MEMS: theory and operation", Electrical and Computer Engineering, 2005. Canadian Conference May 2005 pp.1517-1520, 1-4.

[13] M. Mirzaee, B. S. Virdee, "Realisation of highly compact planar lowpass filter for UWB RFID applications", Electron. Lett., 2013, 49, (22), pp. 1396–1398.

[14] M. Daneshmand,: 'Multi-Port RF MEMS Switches and Switch Matrices', Ph.D. thesis, The University of Waterloo, 2006.

[15] Varadan, V. K., Vinoy, K. J., Jose, K. A.: 'RF MEMS and Their Applications' (John Wiley & Sons Ltd, The Atrium, Southern Gate, Chichester, West Sussex PO19 8SQ, England, 2003).

[16] Rebeiz, G. M.: 'RF MEMS: Theory, Design, and Technology' (John Wiley & Sons, 2003.

Chapter 7

Conclusion and Future Work

A new method to implement low cost chipless RFID tags using MEMS technology is presented in this work. The proposed tags is fabricated using a basic MEMS fabrication process. The elimination of the chip, which accounts for the major portion of the RFID tag costs, can reduce the tag price to become an alternative to barcode labels. Simulation results using a 3-bit chipless tag indicate that the tag can backscatter the signal transmitted by an RFID interrogator. The employed MEMS switches can also be programmed to ensure that each tag has a unique backscattering pattern or identification code. The 3-bit MEMS chipless tag is tested using E5061B 100k-3GHz ENA Series Network Analyzer and probe station form SEMIPORBE^{TM}. For future work a commercial sample of the tag together with a customized antenna and MEMS fuses can be implemented.

A constant path delay Rotman Lens with low phase error is presented in chapter three and four to reduce the design complexity of Rotman lens and enhance its performance

parameters. The implemented lens exhibits a good insertion loss, return loss, and shows phase error as small as 0.45^{o} in the worst-case scenario. A wide bandwidth array patch antenna combined with the proposed Rotman lens is designed to support location positioning. A high gain and directivity microstrip patch antenna array is implemented using $\lambda/4$ microstrip transmission lines. To lower the cost of fabrication and test process, four radial stubs are employed as virtual ground to terminate dummy ports. A 60-GHz RFID reader using passive mixer is presented which utilizes the antenna array and the beamformer for wireless communication. The proposed scheme supports low cost and compact RFID reader implementation.

Tag collision in RFID systems can happen when multiple tags are simultaneously energized by RFID readers. As a future work chipless tag interrogation can be examined to develop a robust solution for the collision problem. Although there are a few proposed solutions in the literature but a practical and cost effective solution requires further studies.

APPENDIX

List of Publications

Published Journal Paper:

1. N. Kandalaft, A. Attaran, R. Rashizadeh,"High Speed Test Interface Module Using MEMS Technology", Microelectronics Reliability, Elsevier, Feb 2015.

2. A. Attaran, R. Rashidzadeh, and R. Muscedere, "Chipless RFID tag using RF MEMS switch" *Electronics Letters* , vol.50, no.23, pp.1720,1722, Nov 2014.

3. A. Attaran and S. Chowdhury, "Fabrication of a 77 GHz Rotman Lens on a High Resistivity Silicon Wafer Using Lift-Off Process," International Journal of Antennas and Propagation, vol. 2014, Article ID 471935, 9 pages, May 2014.

4. A. Attaran, S. Nikan, M. Razzaghpour, "CMOS Class AB Power Amplifier Linearization by Feed Forward Technique for Wireless Communications",

International Review on Communications Antenna and Propagation (IRECAP) Journal, Praise Worthy Prize, vol. 1, no. 1, pp. 29-33, Feb 2011.

Published Conference Paper:

1. V. Mashkovtsev, A. Attaran, and R. Rashidzadeh "DLL Based Test Solution for Interposers in 2.5-D ICs", IEEE International Symposium on Circuits and Systems, May 24-27, 2015. (In press)
2. A. Dianat, A. Attaran, and R. Rashidzadeh "Test Method for Capacitive MEMS Devices Utilizing Pierce Oscillator", IEEE International Symposium on Circuits and Systems, May 24-27, 2015. (In press)
3. A. Attaran, R. Rashidzadeh, and R. Muscedere, Chipless Radio Frequency Identification Tag Using RF MEMS Switches, TEXPO 2014, CMC Microsystems Annual Symposium in Gatineau, Québec on October 6-7, 2014.
4. A. Attaran, S. Chowdhury, "High Performance Silicon Based Rotman Lens for Automotive Radar Applications", CCECE2014 IEEE, May 2014. Paper won the **Second Best Student Paper Award** of the 27th CCECE and invited to their journal for publishing my paper.
5. A. Dianat, A. Attaran, R. Rashidzadeh, and R. Muscedere, "Resonant-Based Test Method for MEMS Devices", ICECS 2014. (In press)

6. A. Attaran, S. Chowdhury, MEMS Radar for Smart Vehicles, Auto21 Annual Conferences, May 29, 2012.

7. A. Attaran, S. Chowdhury, 77GHz Radar for Smart Vehicles, OCE Discovery Annual Conferences, May 15, 2012.

8. I. Hamieh, A. Attaran, S. Chowdhury, A 77 GHz Reconfigurable Micromachined Microstrip Antenna Array, TEXPO 2011, CMC Microsystems Annual Symposium in Gatineau, Québec, Oct. 19-20, 2011.

9. A. Attaran S. Chowdhury, A 77 GHz Micromachined Rotman Lens for Automotive Radar, TEXPO 2011 CMC Microsystems Annual Symposium in Gatineau, Québec on October 19-20, 2011.

Submitted Journal Paper:

1. A. Attaran, R. Rashidzadeh, and R. Muscedere, "Rotman Lens Phase Error Reduction Using Constant Path Delay", International Journal of RF and Microwave Computer-Aided Engineering, Wiley. (Submitted Feb 2015)
2. A. Attaran, R. Rashidzadeh, and R. Muscedere, "Low Phase Error Microwave Lens with Wide Bandwidth Antenna Array for 60GHz RFID Application", International Journal of Microwave and Wireless Technologies, Cambridge University Press. (Submitted Dec 2014, passed the first review)

3. A. Attaran, R. Rashidzadeh, and R. Muscedere, "Novel 60-GHz Millimeter-Wave Identification Reader Using Passive Mixer", Microelectronics Journal, Elsevier. (Submitted May 2014)

4. Attaran, R. Rashidzadeh, and R. Muscedere, "Programmable Chipless Radio Frequency Identification Tag Using RF MEMS Switches" submitted to Microwave Theory and Techniques, IEEE Transactions on, 24pp. (To be submitted)

Book Chapter, Patent

1. A. Attaran, R. Rashidzadeh, Designing EM Waves & Radiating Systems II lab manuscript using 3D software from Agilent called EMPro, summer 2013.

2. Worked on the Rotman lens in the MEMS lab that is part of 77GHz MEMS Radar for Smart Vehicles. US patent is registered by Dr. Sazzadur Chowdhury, application number: 20130027240, January 2013.

VITA AUCTORIS

Ali Attaran received the B.Sc. and M.Sc. degrees in electrical engineering in 2005 and 2008 in Iran and is currently pursuing his Ph.D. degree in electrical engineering at University of Windsor, Windsor, ON, Canada. RFID, Radar, Analog, Digital, RF and Microwave Integrated Circuit Design, MEMS are his research interests.